



Three-dimensional bifurcations in a cubic cavity due to buoyancy-driven natural convection

Tony Wen-Hann Sheu^{a,b,c,*}, Reui-Kuo Lin^{a,1}

^a Department of Engineering Science and Ocean Engineering, National Taiwan University, No. 1, Sec. 4, Roosevelt Road, Taipei 10617, Taiwan, ROC

^b Taida Institute of Mathematical Science (TIMS), National Taiwan University, Taiwan

^c Center for Quantum Science and Engineering (CQSE), National Taiwan University, Taiwan

ARTICLE INFO

Article history:

Received 29 January 2010

Received in revised form 18 August 2010

Accepted 18 August 2010

Available online 18 October 2010

Keywords:

Buoyancy-driven

Limit cycle

Hopf bifurcation

Frequency-doubling bifurcations

Quasi-periodic bifurcation

ABSTRACT

Rich and complex buoyancy-driven flow field due to natural convection will be studied numerically over a wide range of Rayleigh numbers in a cubic cavity by virtue of the simulated bifurcation diagram, limit cycle, power spectrum and phase portrait. When increasing the Rayleigh number, the predicted flow is found to evolve from the conductive state to the state with the onset of convection, which is featured with the steady and symmetric laminar solution, and then to the asymmetric state (pitchfork bifurcation), which will not be discussed in this paper. As the Rayleigh number was further increased, a limit cycle branching from the fixed point of the investigated dynamical system is observed. Supercritical Hopf bifurcation is confirmed to be the birth of the orbitally stable limit cycle that separates the vortex flow into an inner unstable region (moving away from the vortex coreline) and an outer stable region (moving towards the vortex coreline). As the Rayleigh number is increased still, the investigated buoyancy-driven flow became increasingly destabilized through quasi-periodic bifurcation and then through two predicted frequency-doubling bifurcations. Thanks to the power spectrum analysis, bifurcation scenario was confirmed to have an initially single harmonic frequency, which is featured with a driving amplitude. Then an additional ultraharmonic frequency showed its presence. Prior to chaos, in the five predicted arithmetically related frequencies there exists one frequency that is incommensurate to the other two fundamental frequencies. This computational study enlightens that the investigated nonlinear system, which involves frequency-doubling bifurcations, loses its stability to a quasi-periodic bifurcation featured with the formation of a subharmonic frequency. Subsequent to the formation of three frequency-doubling bifurcations and one quasi-periodic bifurcation, an infinite number of frequencies was observed in flow conditions with the continuously increasing Rayleigh numbers. Finally, the chaotic attractor was predicted to be evolved from the strange attractor in the corresponding phase portraits.

© 2010 Elsevier Ltd. All rights reserved.

1. Introduction

In a wall-bounded cavity subject to gravity, convection can be set in when the prescribed temperature difference between the two opposing vertical walls exceeds a critical Rayleigh number. The resulting onset of convective instability and its subsequent transition to periodic, non-periodic, and chaotic states in a three-dimensional (3-D) thermally driven cavity are relevant to crystal growth processes. One major issue that continues to challenge the crystal growth processing engineers is to clarify the occurrence

of layers of impurity, which can normally destroy the crystal homogeneity [1]. Characterization of different thresholds and flow regimes of different physical natures becomes thus an essential issue in the design of a proper crystal growth process.

There have been several noteworthy computational studies of flow transition from the motionless conductive state to the onset of convection due to buoyancy force. Two-phase Rayleigh–Bénard convective problem was considered by Chang and Brown [2]. For a molten fluid, it was shown that an imperfectly deformed boundary could alter the stability characteristics of the fluid flow. Baumgartl et al. [3] studied the case with side-wall thermal boundary conditions pertinent to the Bridgman growth in a vertical cylinder. Roux et al. [4] and Hadid and Roux [5] investigated the unsteady buoyant and thermo-capillary-driven flow at low Prandtl numbers (Pr) in a horizontal Bridgman system to address the effect of Grashof number (Gr) on the developing flow structure and stability. Beyond the critical Rayleigh number (Ra), the time-varying

* Corresponding author at: Department of Engineering Science and Ocean Engineering, National Taiwan University, No. 1, Sec. 4, Roosevelt Road, Taipei 10617, Taiwan, ROC. Tel.: +886 2 33665746; fax: +886 2 23929885.

E-mail addresses: twshsheu@ntu.edu.tw (T.W.-H. Sheu), rklin@ttfri.narl.org.tw (R.-K. Lin).

¹ Tel.: +886 2 23219660x110; fax: +886 2 23211722.

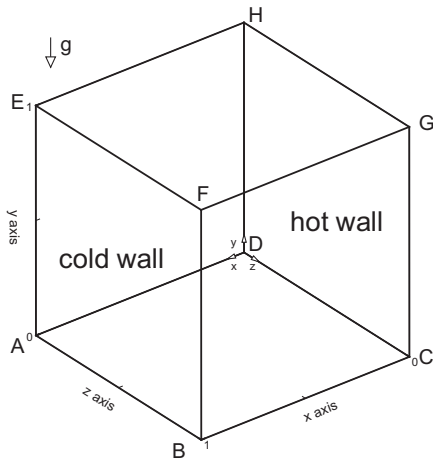


Fig. 1. Schematic of the investigated three-dimensional thermal driven cavity problem with one vertical hot wall (DCGH) and one cold wall (ABFE) at the opposite side. The other four walls are assumed to be adiabatic. Note that $(0, -g, 0)$ is the gravity vector.

flow field may furthermore lose its stability to exhibit a transcritical or a Hopf bifurcation.

Supercritical Hopf bifurcation was reported to appear in the flow driven by solutal gradient within a vertical Bridgman system [6]. Lan and Yang [7] extended their previous work to the study of bifurcating and oscillatory flows in a horizontal Bridgman furnace, from which a supercritical Hopf bifurcation was observed to appear at an intermediate Rayleigh number. Within the time periodic flow regime, they showed that the interface, which was shown to temporally oscillate, could lead to crystal striations. Flow bifurcation in a vertical cylinder heated from below was also investigated by Yamaguchi et al. [8] and Ma et al. [9], who found multiple steady-state flows at different Rayleigh numbers and aspect ratios. A notable recent work is the study of 3-D axisymmetry-breaking instabilities in a destabilized Bridgman-like configuration using the linear stability analysis by Gelfgat et al. [10]. Pulicani et al. [11] and Bennacer et al. [12] have shown that in their investigated thermal cavity the instabilities caused by some more elongated cells would break the basic roll into several cells. On the other hand, fluids in a cavity of smaller aspect ratios require a large

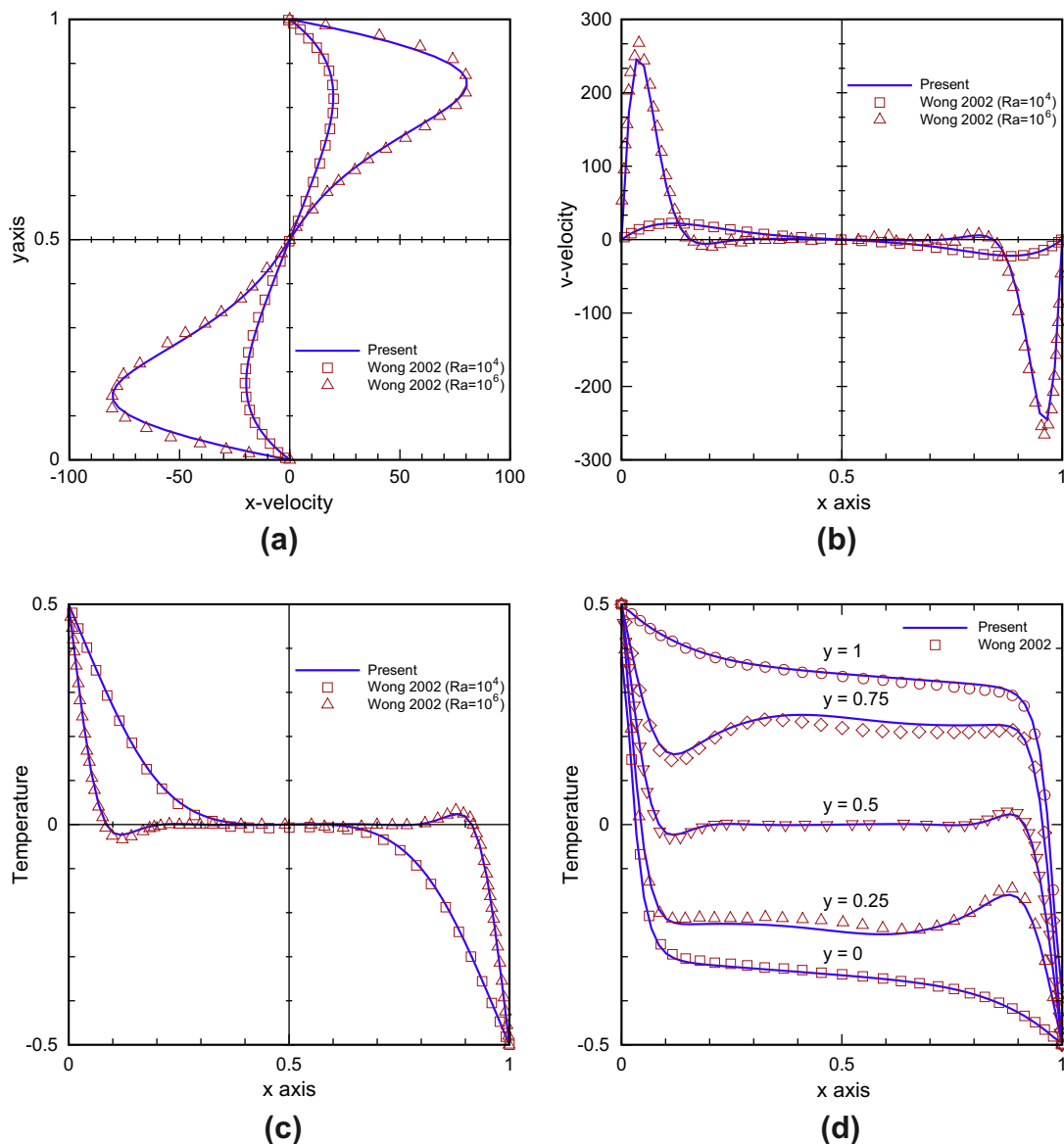


Fig. 2. The predicted velocity and temperature profiles along the centerline of the plane $z = \frac{1}{2}$ at $Ra = 10^4$ and 10^6 for the comparison sake. (a) Velocity u profiles $u(0, y, \frac{1}{2})$; (b) velocity v profiles $v(x, 0, \frac{1}{2})$; (c) temperature T profiles $T(x, 0, \frac{1}{2})$; (d) temperature T profiles at various y -locations.

buoyancy force to make the resulting flow field become unstable [13].

According to Elder [14] and Seki et al. [15], the convective flow in a cubical cavity becomes unstable along with the developed small disturbances. Guckenheimer and Holmes [16] and Wiggins [17] have analyzed these 3-D disturbances based on the Hopf bifurcation theory to highlight the existence of limit cycles. In the literatures it has been investigated so far the structure of limit cycles, resulting from an externally modulated Rayleigh–Bénard system [18], the nonlinear damping coefficient [19], and the effect of induction machine load [20]. Also, a successive transition from the primary convective steady-state to the oscillatory motion and, finally, to the chaotic motion has been the subject of several recent works of Pulicani et al. [11], Le Quere and Behnia [21], Gelfgat et al. [10] and Xin and Le Quere [22].

The aim of the current investigation is to numerically investigate the fascinating bifurcation phenomenon in the cavity under the condition that the two fixed temperatures, one is specified at the vertical wall (hot) and the other is at the opposing cold wall, were imposed on the opposite vertical walls. The rest of the walls

were assumed to be adiabatic as shown in Fig. 1. Simulation of the equations for mass, momentum and energy conservations was conducted along with the prescribed no-slip velocity boundary condition and subject to the divergence-free initial condition. This study will, in particular, focus on the periodic oscillations and aperiodic or chaotic motions with the increasing Ra for illustrating the supercritical bifurcation nature. In addition, a branch of quasi-periodic solutions will be elucidated at a time subsequent to the presence of periodic bifurcations.

In the cubical cavity, the legitimate bifurcation analysis which goes beyond the linear stability analysis will be conducted to clarify some possibly involved flow/thermal bifurcations. The nature of these bifurcations, arising from the developing disturbances, was deliberated by virtue of the limit cycle oscillation theory [23]. The route to chaos by way of Hopf and pseudo periodic bifurcations occurring in the current dynamical system will be also rigorously revealed and analyzed. Transition to chaos has been commonly characterized by its power spectrum. Hakin [24] used the Lyapunov exponents and Grassberger and Procaccia [25] used the correlation dimension to distinguish various attractors quantitatively.

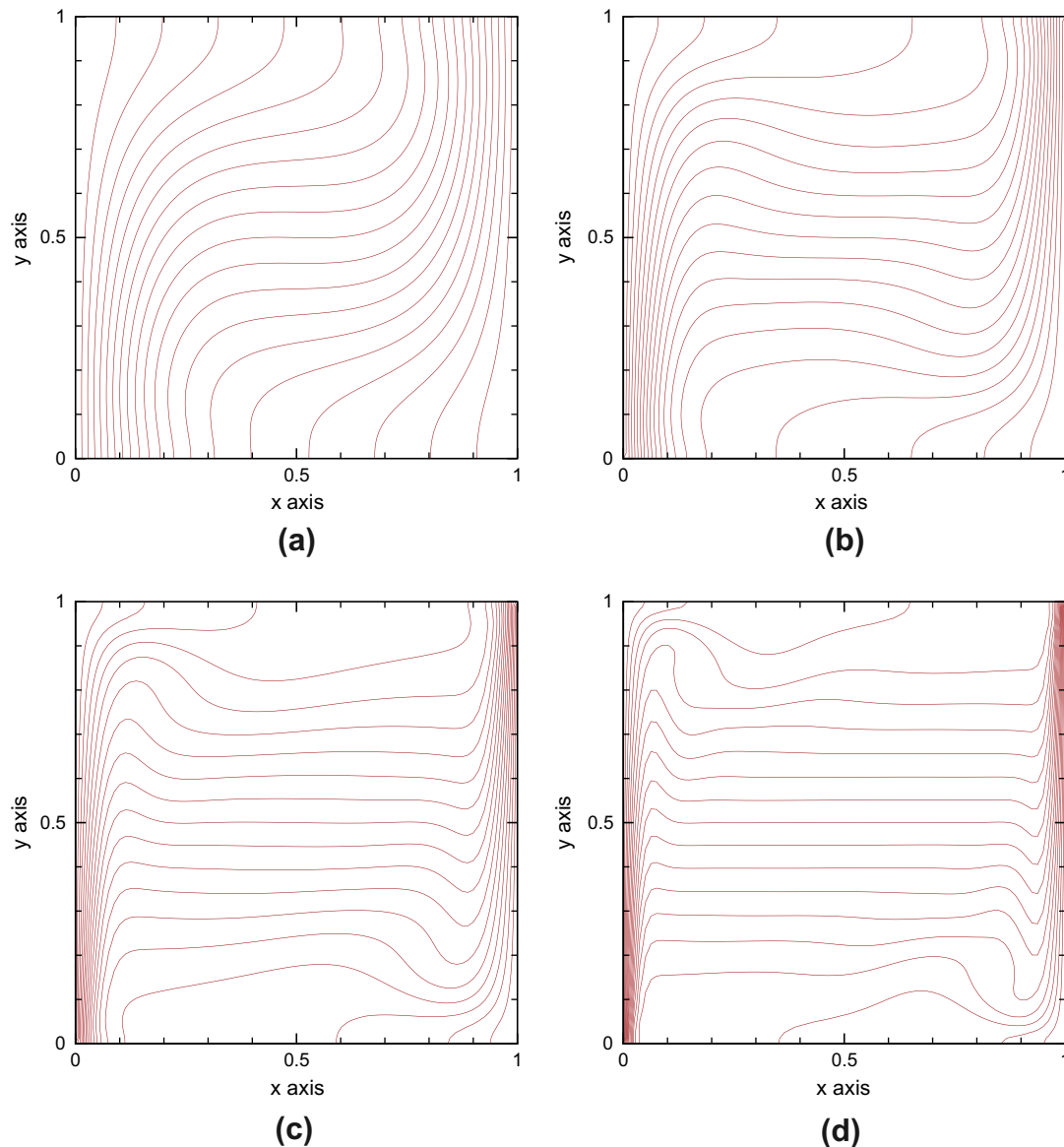


Fig. 3. The predicted temperature contours on the plane of symmetry at different values of Ra . (a) 10^4 ; (b) 1.6×10^5 ; (c) 10^6 ; (d) 1.6×10^7 .

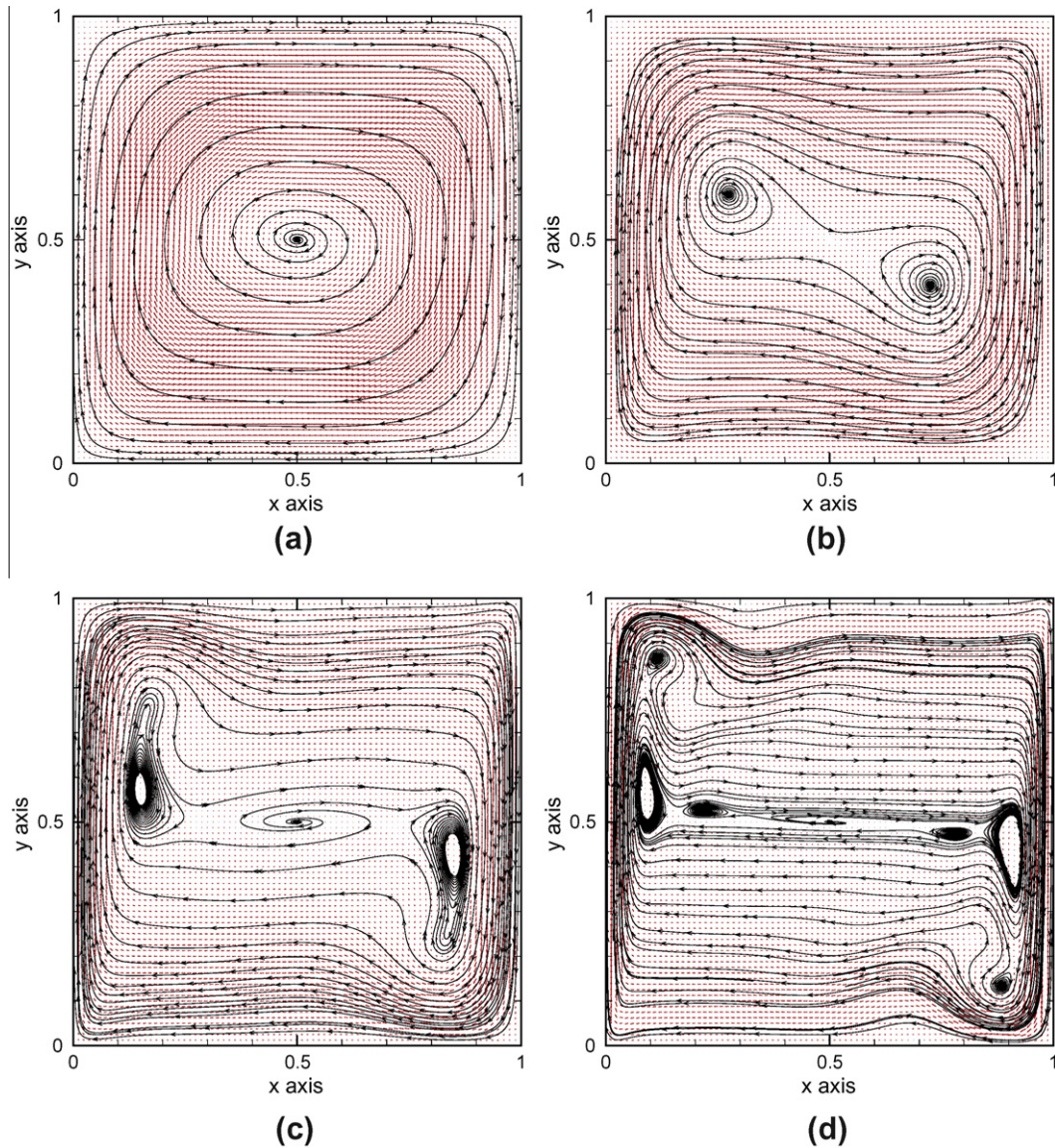


Fig. 4. The predicted streamlines on the plane of symmetry. (a) $Ra = 10^4$; (b) $Ra = 1.6 \times 10^5$; (c) $Ra = 10^6$; (d) $Ra = 1.6 \times 10^7$.

Table 1
Comparison of the predicted and referenced solutions for the case investigated at $Ra = 10^6$.

Grid	Ref. [33]	Ref. [34]	Ref. [35]	Ref. [36]	Ref. [37]	Present work	
	$33 \times 33 \times 29$	62^3	120^3	27^3	81^3	61^3	81^3
u_{\max}				127.75	126.97	127.031	126.943
v_{\max}	234.3			239.33	236.72	237.562	236.921
w_{\max}	23.5			25.15	25.56	25.322	26.498
$u_{\text{mp,max}}$		70.914	68.245		68.21	68.323	68.207
$v_{\text{mp,max}}$		218.068	217.815		217.47	217.548	217.493
Nu_{mp}		9.012		8.876	8.877	8.881	8.879
$Nu_{3D,v}$	8.61	8.770	8.639	8.634	8.640	8.672	8.641

Study of the evolving stability in this study was based on the predicted time series solutions, including their power spectra and phase portraits.

The rest of this paper is organized as follows. The problem with the boundary conditions that lead to flow symmetry with respect to the y -plane was described in Section 2. This is followed by the presentation of divergence-free compensated method employed to solve the incompressible viscous flow equations and the

optimized dispersion discretization scheme used to approximate the convective terms in non-staggered grids. Description of the problem is then given in Section 3. Prior to the discussion of the predicted results, we conduct numerical validation of the proposed scheme and the solution algorithm presented in Section 4. The results and discussion are then given in Section 5 with the emphasis on the bifurcation route to chaos. The paper will be concluded with some remarks in Section 6.

2. Problem description

A Boussinesq fluid of Prandtl number $Pr (\cong 0.71)$ was investigated in a 3-D cubical cavity ($0 \leq x, y, z \leq 1$), which was subject to the hot wall condition at the temperature $T_h(x = 0, y, z) = \frac{1}{2}$ and the cold wall condition at the temperature $T_c(x = 1, y, z) = -\frac{1}{2}$. All the velocity boundary conditions were assumed to be of the no-slip type. Both of the thermal and hydrodynamic properties for the melt fluid under current investigation were treated as constants. The working fluid was considered to be incompressible and Newtonian along with the Boussinesq approximation being assumed in the equations of motion. The resulting governing equations in the gravitational field $\mathbf{g} = (0, -g, 0)$ are given below

$$\nabla \cdot \mathbf{v} = 0 \tag{1}$$

$$\frac{\partial \mathbf{v}}{\partial t} + (\mathbf{v} \cdot \nabla) \mathbf{v} = -\nabla p + Pr \nabla^2 \mathbf{v} + Ra Pr T \vec{e}_y \tag{2}$$

$$\frac{\partial T}{\partial t} + (\mathbf{v} \cdot \nabla) T = \nabla^2 T \tag{3}$$

In the above equations, $\mathbf{v} = (u, v, w)$, t , p and T represent the velocity vector along the (x, y, z) directions, time, pressure and temperature, respectively. Two dimensionless parameters known as the Prandtl number $Pr = \nu/\alpha$ and the Rayleigh number $Ra = (g\beta_T \Delta T L^3)/(\nu\alpha)$, where ν , α and β_T denote the viscosity, thermal diffusivity and the coefficient of thermal expansion, are involved in the investigated dimensionless nonlinear differential system.

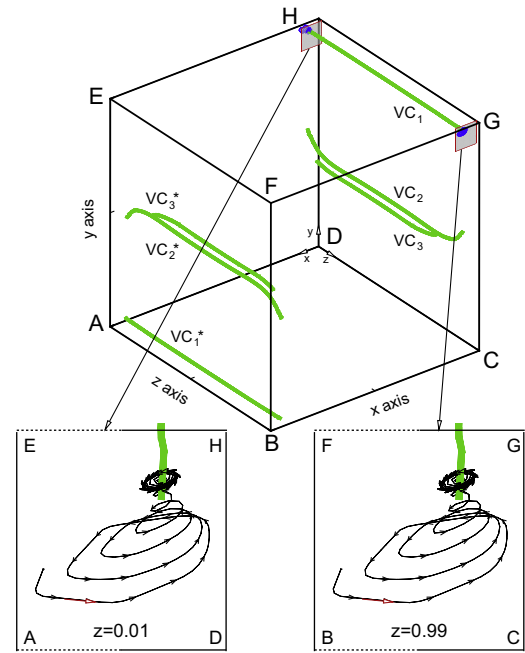


Fig. 6. The predicted two sets of vortical corelines in the cavity due to thermally driven flow motion at $Ra = 1.233 \times 10^8$. Limiting streamlines near two ends of the vortical coreline VC_1 are plotted to reveal the formation of VC_1 from the inward spiralling particle motions at the two vertical walls $z = 0.01$ and $z = 0.99$.

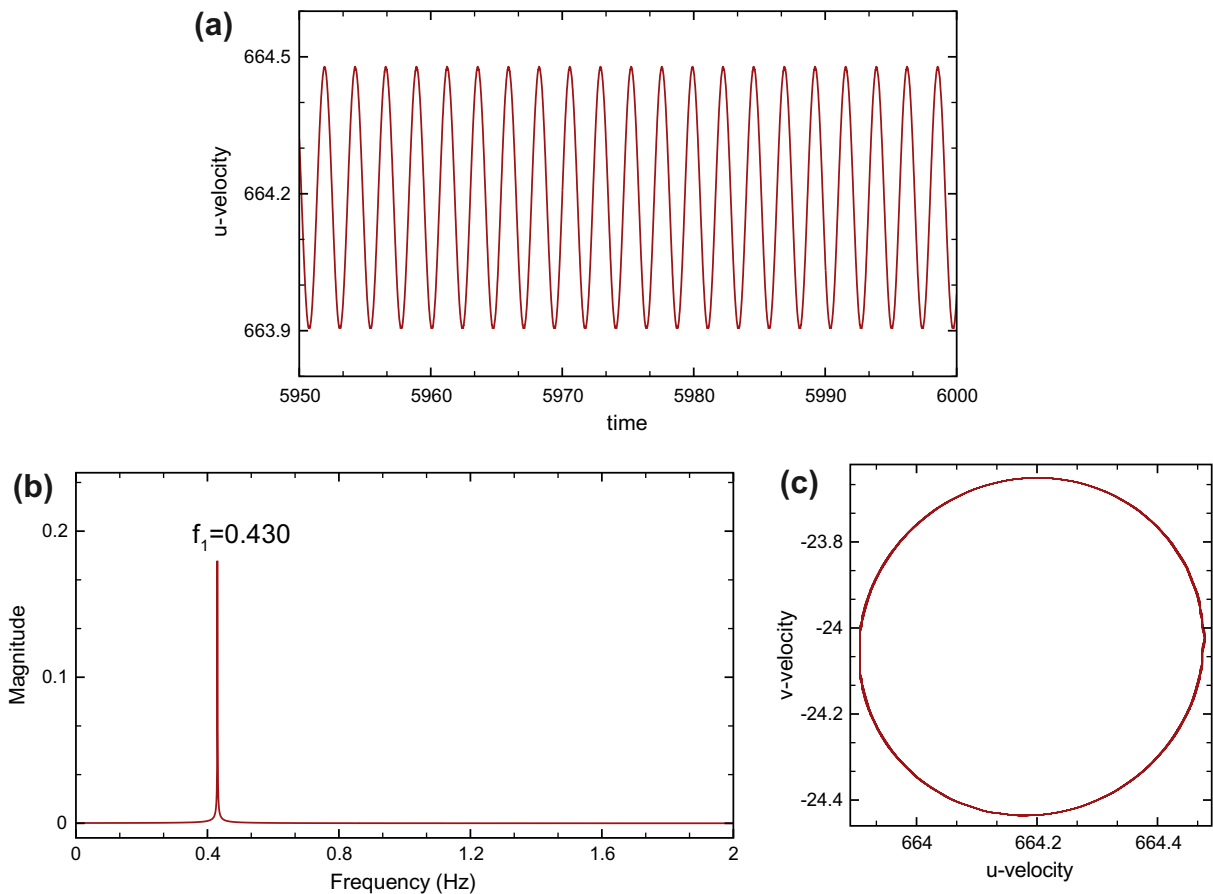


Fig. 5. The power spectrum of the predicted u -velocity component at the chosen point $(x, y, z) = (0.9, 0.9, 0.9)$, where the primary frequency is $f_1 \approx 0.430$ Hz, for the case investigated at $Ra_p = 1.233 \times 10^8$. (a) Time-evolving x -component velocity u ; (b) FFT plot; (c) limit cycle.

One of the main aims of conducting the present numerical study was to know the qualitative behavior of the buoyancy induced flowfield by determining the number of critical points (including the fixed point, limit cycle, and quasi-periodic (or chaotic) orbit) and separatrices (including the lines of separation and attachment) existing in the velocity vector field. Another aim of primary importance in this study is to know which of these non-wandering sets were stable, thereby prompting the stability analysis of the non-wandering sets. Flow stability can be either of a weaker (Lyapunov stability) or a stronger (asymptotic stability) type. An orbit remaining all the time in the neighborhood of a non-wandering set is called the Lyapunov stability. Every orbit in the neighborhood of a non-wandering set that approaching the same set asymptotically is known as the asymptotic stability. Another important subject to be discussed in this study is the correlation between the number of non-wandering sets and the control parameter, which is Ra in the nonlinear system of current interest. The appearance and disappearance of non-wandering set is called

bifurcation. Knowledge about the changes in flow stability and bifurcation, which always coincide in nonlinear dynamics, is thus crucial to get a better understanding of the currently investigated nonlinear differential system. Another main objective in conducting this study is to explore the hydrodynamic and thermal details based on the topology theory.

3. Numerical method

Within the current fractional-step formulation, calculation of the time-dependent Navier–Stokes equations can be decomposed into two steps based on the Helmholtz–Hodge decomposition theorem [26]. Along with this underlying theory, we are led to know that there exist a vector field \mathbf{w} , which can be decomposed into a solenoidal field with its zero normal component on the boundary, and the gradient of some scalar functions. We can, as a result, assign the scalar function as p and the divergence-free vec-

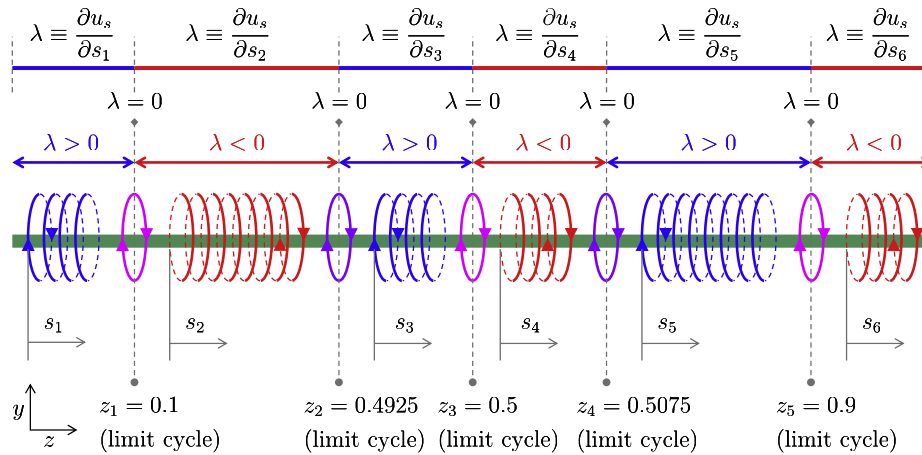


Fig. 7. The cartoon plot of the predicted spiralling particle motion in flow regions adjacent to the vortical coreline VC_1 . Five limit cycles (represented by purple color) are predicted at the locations where $\lambda = 0$ (or at locations $z = 0.1, 0.4925, 0.5, 0.5075, 0.9$ where the values of λ change sign) along the entire VC_1 coreline (represented by green line). Note that red and blue colored particle lines represent the left-running ($\lambda < 0$) and right-running ($\lambda > 0$) spiralling particle motions, respectively. (For interpretation of the references to colour in this figure legend, the reader is referred to the web version of this article.)

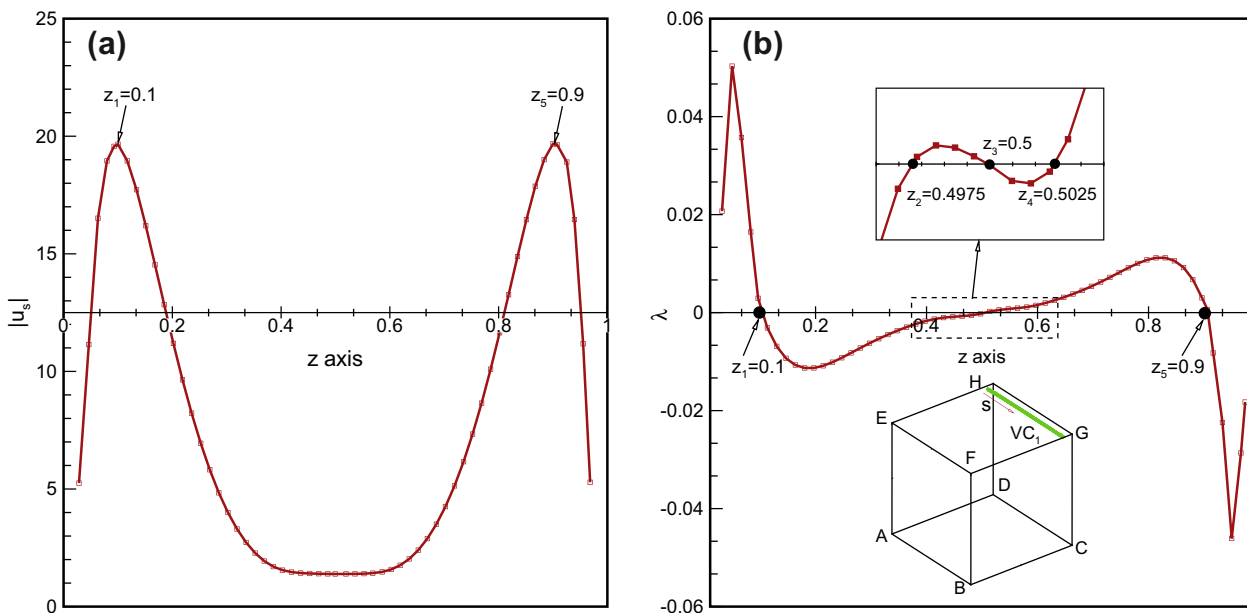


Fig. 8. Along the vortical coreline VC_1 , (a) $|u_s|$ is plotted against z -axis; (b) $\lambda (\equiv \frac{\partial u_s}{\partial s})$ is plotted against the coordinate s schematic in the figure.

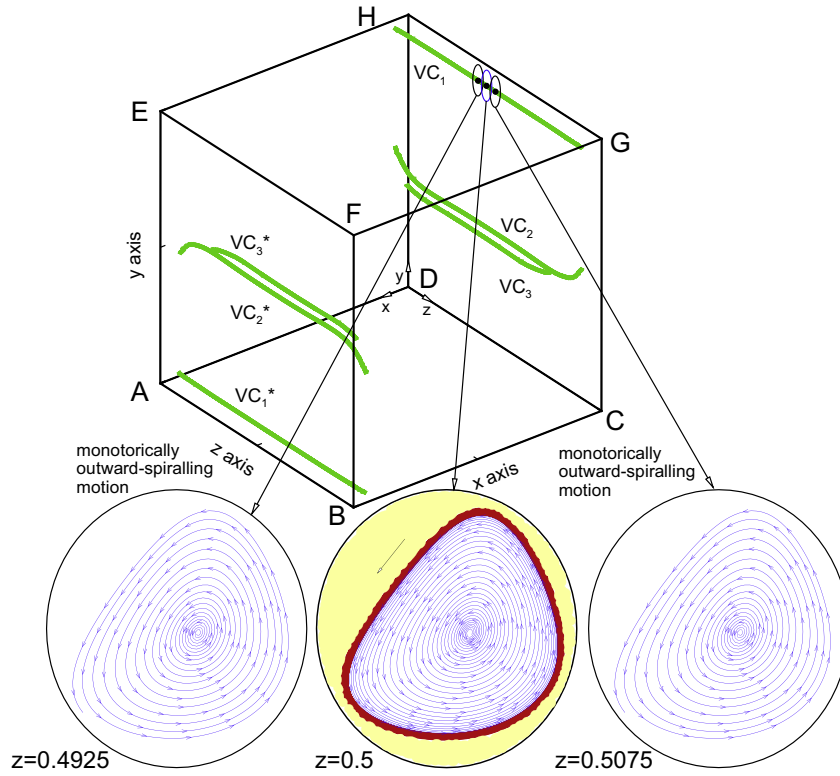


Fig. 9. Particle motions at the chosen three cross-flow planes ($z = 0.4925, 0.5$ and 0.5075). Note that the regions with yellow and white colors represent the particle spiralling inwards and outwards, respectively. At the cutting plane $z = 0.5$, the closed curve between the blue and red regions denotes the limit cycle formation (represented by red color).

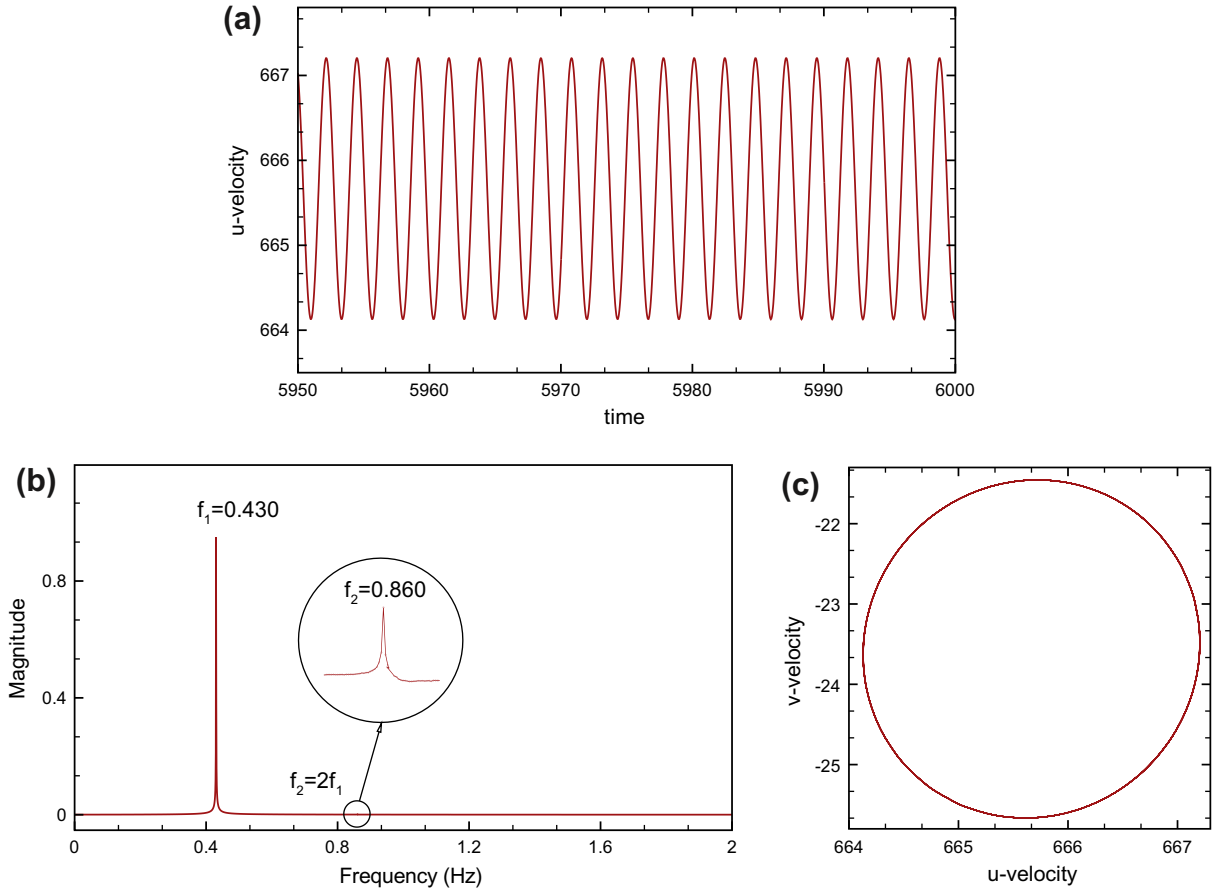


Fig. 10. The power spectrum of the predicted u -velocity component at the chosen point $(x, y, z) = (0.9, 0.9, 0.9)$, where the primary and secondary frequencies are $f_1 \approx 0.430$ Hz and $f_2 \approx 0.860$ Hz, for the case investigated at $Re_{FD1} = 1.235 \times 10^8$. (a) Time-evolving x -component velocity u ; (b) FFT plot; (c) limit cycle.

tor field as \mathbf{v} . The chosen projection operator P maps the vector \mathbf{w} onto its divergence-free vector field \mathbf{v} , where $\mathbf{v} = \mathbf{w} - \nabla p$. This is followed by applying the projection operator P to render $P\mathbf{w} = P\mathbf{v} + P(\nabla p)$. According to the definition of P , we will get $P\mathbf{w} = P\mathbf{v} = \mathbf{v}$ and, in turn, $P(\nabla p) = 0$. The differential operator P is then applied to both sides of Eq. (2) to yield $P\frac{\partial \mathbf{v}}{\partial t} = P[-(\mathbf{v} \cdot \nabla)\mathbf{v} - \nabla p + Pr\nabla^2\mathbf{v} + RaPrT\vec{e}_y]$. Since \mathbf{v} is a divergence-free vector, we are led to get $P(\frac{\partial \mathbf{v}}{\partial t}) = \frac{\partial \mathbf{v}}{\partial t}$ or $\frac{\partial \mathbf{v}}{\partial t} = P[-(\mathbf{v} \cdot \nabla)\mathbf{v} - \nabla p + Pr\nabla^2\mathbf{v} + RaPrT\vec{e}_y]$.

The intermediate velocity $\mathbf{v}^{n+\frac{1}{2}}$ can be therefore calculated from the following fully implicit equation along with the prescribed no-slip velocity with the pressure term being eliminated from the momentum equations

$$\frac{\mathbf{v}^{n+\frac{1}{2}} - \mathbf{v}^n}{\Delta t} = -(\mathbf{v}^{n+\frac{1}{2}} \cdot \nabla)\mathbf{v}^{n+\frac{1}{2}} + Pr\nabla^2\mathbf{v}^{n+\frac{1}{2}} + RaPrT^{n+\frac{1}{2}}\vec{e}_y \quad (4)$$

Calculation of the incompressible viscous flow solutions becomes, as a result, much simplified. Through the advection step, given by $\frac{\mathbf{v}_a^{n+\frac{1}{2}} - \mathbf{v}^n}{\Delta t} + (\mathbf{v}^n \cdot \nabla)\mathbf{v}^n = 0$, and the diffusion step, given by $\frac{\mathbf{v}^{n+\frac{1}{2}} - \mathbf{v}_a^{n+\frac{1}{2}}}{\Delta t} = Pr\nabla^2\mathbf{v}^{n+\frac{1}{2}} + RaPrT^{n+\frac{1}{2}}\vec{e}_y$, the predicted intermediate velocity solution $\mathbf{v}^{n+\frac{1}{2}}$ is not necessarily to be divergence-free. The intermediate field $\mathbf{v}^{n+\frac{1}{2}}$ needs, therefore, to be decomposed into the sum of the solenoidal velocity field \mathbf{v}^{n+1} and the gradient of the currently chosen scalar function, which is proportional to the unknown pressure gradient $\Delta t \nabla p^{n+1}$. This enlightens the necessity of employing the projection step, which includes $\frac{\mathbf{v}^{n+1} - \mathbf{v}^{n+\frac{1}{2}}}{\Delta t} = -\nabla p^{n+1}$ and $\nabla \cdot \mathbf{v}^{n+1} = 0$. Calculation of \mathbf{v}^{n+1} needs to know a priori pressure solu-

tion, which can be calculated from the Poisson equation given by $\nabla^2 p = \nabla \cdot \mathbf{v}^{n+\frac{1}{2}}$.

3.1. Derivation of the compensated momentum source term

Substitution of $\frac{\mathbf{v}^{n+1} - \mathbf{v}^{n+\frac{1}{2}}}{\Delta t} + \nabla p^{n+1} = 0$ into the semi-discrete momentum equation yields

$$\frac{\mathbf{v}^{n+1} - \mathbf{v}^n}{\Delta t} + (\mathbf{v}^{n+\frac{1}{2}} \cdot \nabla)\mathbf{v}^{n+\frac{1}{2}} - Pr\nabla^2\mathbf{v}^{n+\frac{1}{2}} + \nabla p^{n+1} = M_1 + M_2 + RaPrT^{n+1}\vec{e}_y \quad (5)$$

where $M_1 = [(\mathbf{v}^{n+\frac{1}{2}} \cdot \nabla)\nabla p^{n+1} + (\nabla p^{n+1} \cdot \nabla)\mathbf{v}^{n+\frac{1}{2}} - Pr\nabla^2(\nabla p^{n+1})]\Delta t$ and $M_2 = -[(\nabla p^{n+1} \cdot \nabla)\nabla p^{n+1}]\Delta t^2$. Let p^{n+1} be $p^* + p'$, the pressure-gradient step can be decomposed into $\frac{\mathbf{v}^* - \mathbf{v}^{n+\frac{1}{2}}}{\Delta t} = -\nabla p^*$ and $\frac{\mathbf{v}^{n+1} - \mathbf{v}^*}{\Delta t} = -\nabla p'$, where p^* is the intermediately predicted pressure. Eq. (5) can, therefore, be reformulated as [27]

$$\frac{\mathbf{v}^{n+1} - \mathbf{v}^n}{\Delta t} + (\mathbf{v}^* \cdot \nabla)\mathbf{v}^* - Pr\nabla^2\mathbf{v}^* + \nabla p^* = -\nabla p' + M_3 + M_4 + RaPrT^{n+1}\vec{e}_y \quad (6)$$

where

$$M_3 = [(\mathbf{v}^* \cdot \nabla)\nabla p' + (\nabla p' \cdot \nabla)\mathbf{v}^*]\Delta t - Pr\nabla(\nabla \cdot \mathbf{v}^*) \quad (7)$$

$$M_4 = -[(\nabla p' \cdot \nabla)\nabla p']\Delta t^2 \quad (8)$$

Define the momentum source term M_{DFC} as $-\nabla p' + M_3 + M_4$. This term is used to replace the divergence-free constraint condition and we can call M_{DFC} as the Divergence-Free Compensated (DFC) momentum source term.

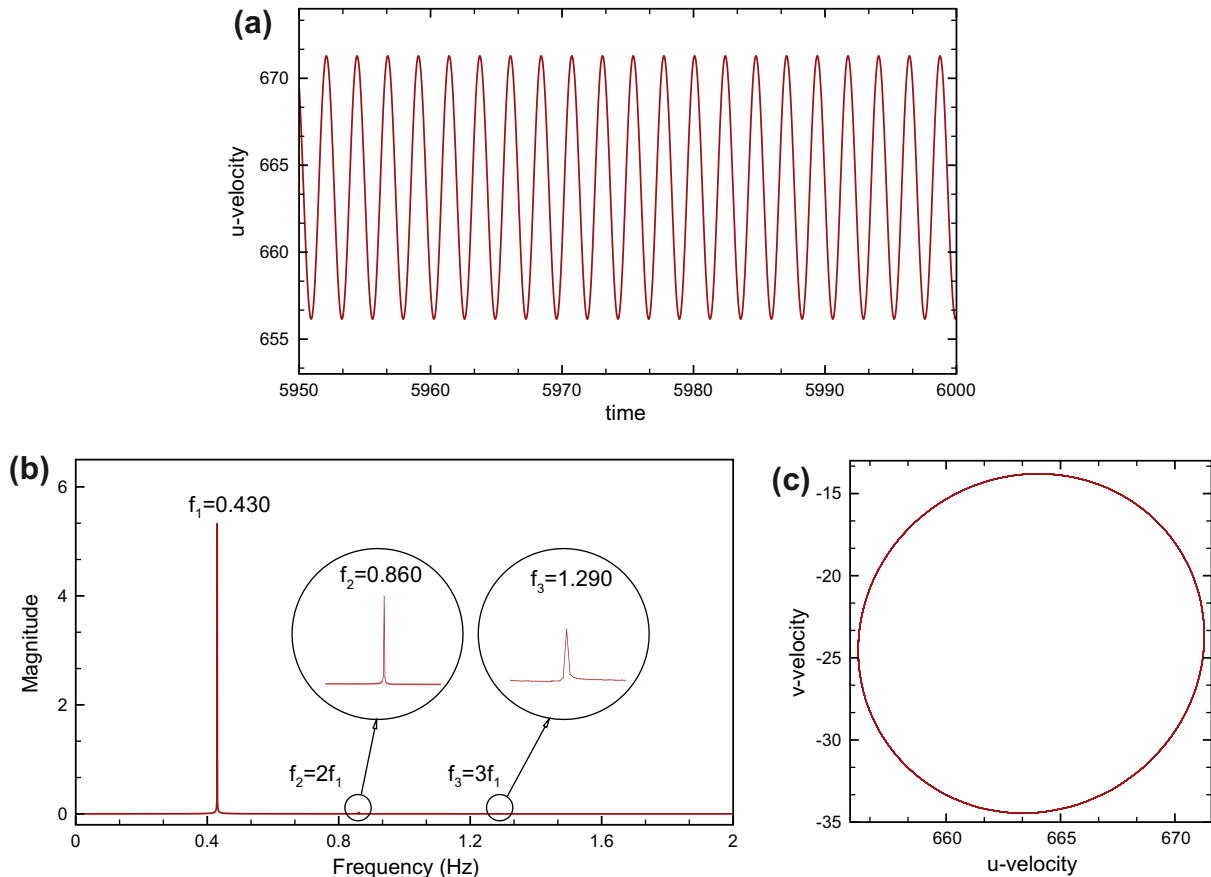


Fig. 11. The power spectrum of the predicted u -velocity component at the chosen point $(x, y, z) = (0.9, 0.9, 0.9)$, where the primary and secondary frequencies are $f_1 \approx 0.430$ Hz, $f_2 = 2f_1 \approx 0.860$ Hz and $f_3 = f_1 + f_2 \approx 1.290$ Hz, for the case investigated at $Ra_{FD_2} = 1.236 \times 10^8$. (a) Time-evolving x -component velocity u ; (b) FFT plot; (c) limit cycle.

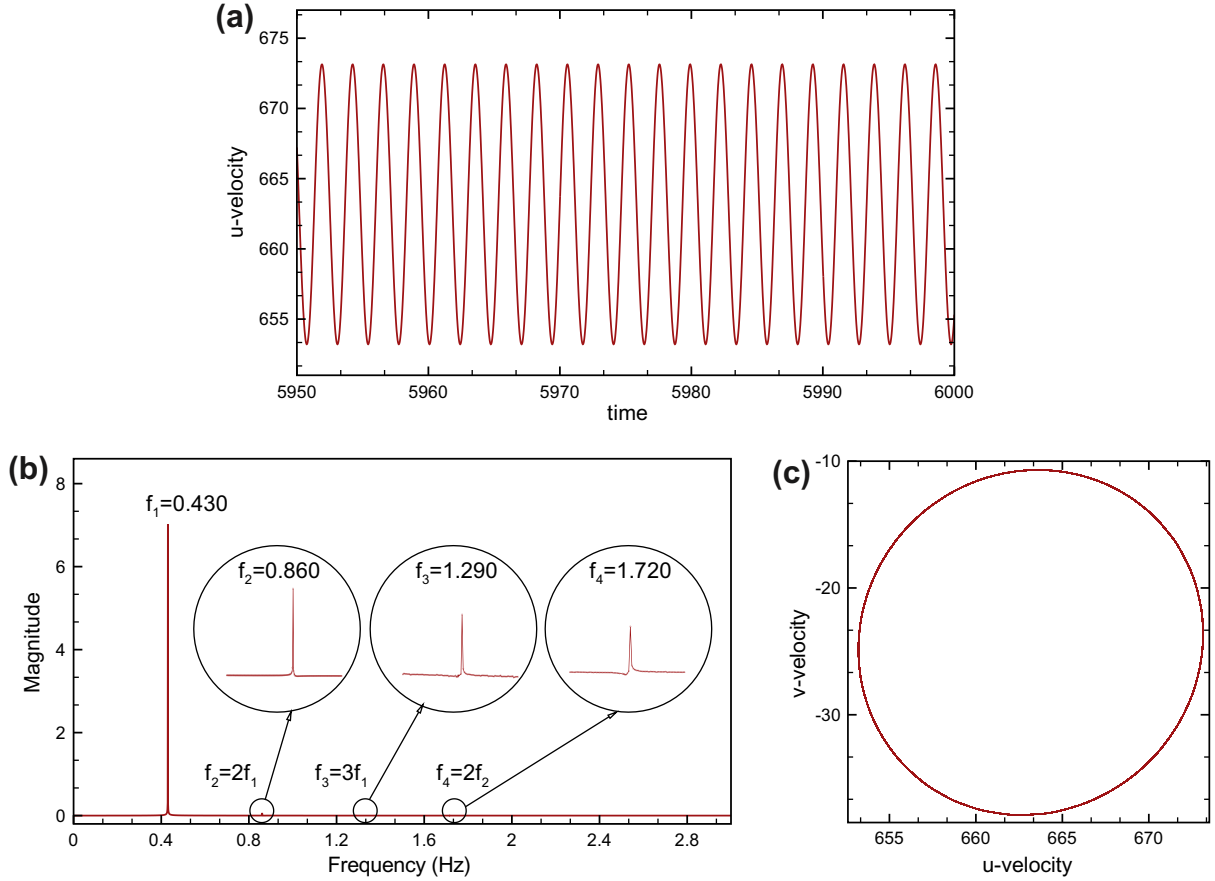


Fig. 12. The power spectrum of the predicted u -velocity component at the chosen point $(x, y, z) = (0.9, 0.9, 0.9)$, where the primary and secondary frequencies are $f_1 \approx 0.430$ Hz, $f_2 = 2f_1 \approx 0.860$ Hz, $f_3 = f_1 + f_2 \approx 1.290$ Hz and $f_4 = 2f_2 \approx 1.720$ Hz, for the case investigated at $Re_{FD_3} = 1.238 \times 10^8$. (a) Time-evolving x -component velocity u ; (b) FFT plot; (c) limit cycle.

3.2. Advection scheme with minimized dispersion error

For the approximation of the convection terms in flow equations, we will extend the previously proposed two-dimensional advection scheme [28] to carry out the current three-dimensional analysis. The spatial derivative term u_x , for example, shown in the momentum equation is approximated as follows:

$$u_x(x, y, z) \simeq \frac{1}{h} (a_1 u_{i-2,j,k} + a_2 u_{i-1,j,k} + a_3 u_{i,j,k} + a_4 u_{i+1,j,k} + a_5 u_{i,j,k-1} + a_6 u_{i,j-1,k} + a_7 u_{i,j+1,k} + a_8 u_{i,j+2,k} + a_9 u_{i,j,k-2} + a_{10} u_{i,j,k-1} + a_{11} u_{i,j,k+1} + a_{12} u_{i,j,k+2}) \quad (9)$$

Expansion of the terms $u_{i\pm 1,j,k}$, $u_{i\pm 2,j,k}$, $u_{i,j\pm 1,k}$, $u_{i,j\pm 2,k}$, $u_{i,j,k\pm 1}$, $u_{i,j,k\pm 2}$ with respect to $u_{i,j,k}$ in Taylor series enables us to get the resulting modified equation. Derivation is followed by eliminating the leading eleven error terms to formulate a coupled system of algebraic equations. For uniquely determining the coefficients a_1 – a_{12} shown above, one more equation needs to be derived. The underlying idea of deriving this algebraic equation is to minimize the dispersion error, which is the difference between the physical and numerical wavenumbers of the first-order spatial derivative, for u_x so as to effectively suppress any erroneous convective oscillation [29].

With this idea in mind, one can manipulate the right hand side of Eq. (9) to get nearly the same Fourier transform in space as the original derivative term shown in the left hand side of Eq. (9). Define firstly the Fourier transform and its inverse for $u(x, y, z)$ in three dimensions as follows:

$$\tilde{u}(\alpha, \beta, \gamma) = \frac{1}{(2\pi)^2} \int_{-\infty}^{+\infty} \int_{-\infty}^{+\infty} \int_{-\infty}^{+\infty} u(x, y, z) e^{-i(\alpha x + \beta y + \gamma z)} dx dy dz \quad (10)$$

$$u(x, y, z) = \int_{-\infty}^{+\infty} \int_{-\infty}^{+\infty} \int_{-\infty}^{+\infty} \tilde{u}(\alpha, \beta, \gamma) e^{i(\alpha x + \beta y + \gamma z)} d\alpha d\beta d\gamma \quad (11)$$

By applying the above Fourier transform to each term shown in Eq. (9), the first component in the actual wavenumber vector $\underline{\alpha} = (\alpha, \beta, \gamma)$ can be derived as

$$\alpha \simeq \frac{-i}{h} (a_1 e^{i(-2zh)} + a_2 e^{i(-zh)} + a_3 + a_4 e^{i(zh)} + a_5 e^{i(-2\beta h)} + a_6 e^{i(-\beta h)} + a_7 e^{i(\beta h)} + a_8 e^{i(2\beta h)} + a_9 e^{i(-2\gamma h)} + a_{10} e^{i(-\gamma h)} + a_{11} e^{i(\gamma h)} + a_{12} e^{i(2\gamma h)}) \quad (12)$$

where $i = \sqrt{-1}$. In an approximated sense, the effective wavenumber component $\tilde{\alpha}$ is defined as

$$\tilde{\alpha} = \frac{-i}{h} (a_1 e^{i(-2zh)} + a_2 e^{i(-zh)} + a_3 + a_4 e^{i(zh)} + a_5 e^{i(-2\beta h)} + a_6 e^{i(-\beta h)} + a_7 e^{i(\beta h)} + a_8 e^{i(2\beta h)} + a_9 e^{i(-2\gamma h)} + a_{10} e^{i(-\gamma h)} + a_{11} e^{i(\gamma h)} + a_{12} e^{i(2\gamma h)}) \quad (13)$$

To make $\tilde{\alpha}$ an appropriate representation of α , the value of $|\alpha h - \tilde{\alpha} h|^2$ should be small and positive in the following weak sense [29–31]:

$$\begin{aligned}
 E(\alpha) &= \int_{-\frac{\pi}{2}}^{\frac{\pi}{2}} \int_{-\frac{\pi}{2}}^{\frac{\pi}{2}} \int_{-\frac{\pi}{2}}^{\frac{\pi}{2}} |\alpha h - \tilde{\alpha} h|^2 d(\alpha h) d(\beta h) d(\gamma h) \\
 &= \int_{-\frac{\pi}{2}}^{\frac{\pi}{2}} \int_{-\frac{\pi}{2}}^{\frac{\pi}{2}} \int_{-\frac{\pi}{2}}^{\frac{\pi}{2}} |\kappa_1 - \tilde{\kappa}_1|^2 d\kappa_1 d\kappa_2 d\kappa_3
 \end{aligned}
 \tag{14}$$

In the above, $(\kappa_1, \kappa_2, \kappa_3) = (\alpha h, \beta h, \gamma h)$.

To make E a minimum value, $\frac{\partial E}{\partial a_4} = 0$ is enforced to enable us to get $a_5 = a_8 = a_9 = a_{12} = -\frac{1}{72} \frac{\pi(-10+3\pi)}{-8+3\pi}$, $a_6 = a_7 = a_{10} = a_{11} = \frac{1}{18} \frac{\pi(-10+3\pi)}{-8+3\pi}$, $a_2 = -1$, $a_3 = -\frac{1}{6} \frac{-19\pi+3\pi^2+24}{-8+3\pi}$, $a_4 = \frac{1}{3}$, and $a_1 = \frac{1}{6}$. In view of the resulting modified equation, the approximated equation for u_x is shown to have a spatial accuracy order of third. Other

two convective terms u_y and u_z can be similarly approximated by the same scheme that preserves the wavenumber relation.

4. Validation study

To validate the present analysis code, the solutions predicted at $Ra = 10^6$ and $Pr = 0.71$ in the currently investigated cubic cavity will be compared with other available numerical results. We present firstly the predicted velocity profiles $u(x, \frac{1}{2}, z)$, $v(\frac{1}{2}, y, z)$ and $T(\frac{1}{2}, y, z)$ at the central plane $z = \frac{1}{2}$. The grid-independent velocity profiles predicted at $\Delta x = \Delta y = \Delta z = \frac{1}{80}$ planes will be compared with the numerically predicted profiles of Wong and Baker [32]

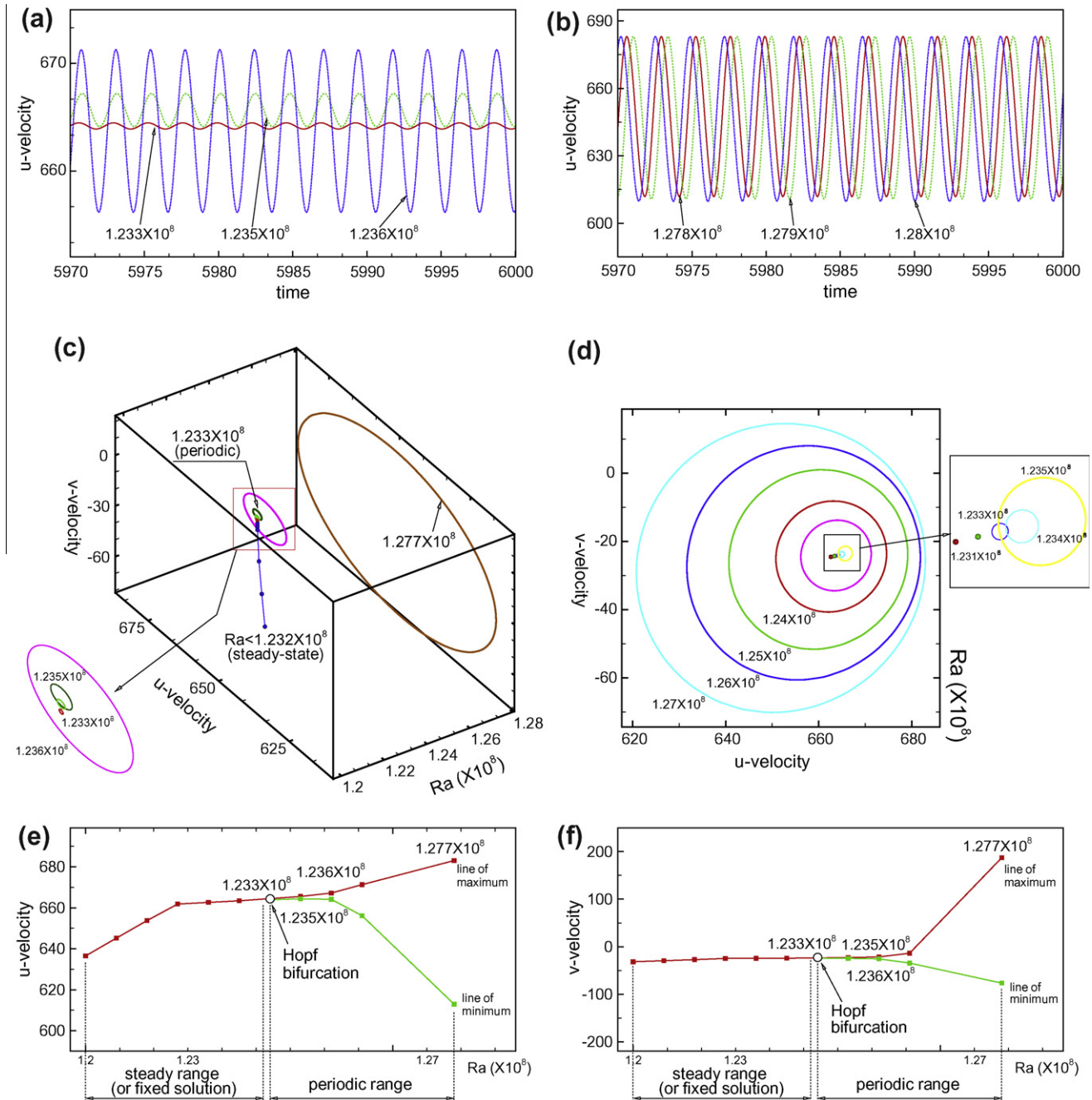


Fig. 13. Summary of the phase portraits predicted in the periodic range of $1.233 \times 10^8 \leq Ra \leq 1.28 \times 10^8$. (a) The predicted time series solutions for u at $Ra = 1.233 \times 10^8$, 1.235×10^8 and 1.236×10^8 ; (b) the predicted time series solutions for u at $Ra = 1.278 \times 10^8$, 1.279×10^8 and 1.28×10^8 ; (c) limit cycles plotted in the (u, v, Ra) coordinates at different values of Ra ; (d) limit cycles plotted in the (u, v, Ra) coordinates at different values of Ra ; (e) plot of u against Ra which falls into the steady and periodic ranges; (f) plot of v against Ra which falls into the steady and periodic ranges.

in Fig. 2(a)–(c). The temperature profiles at various vertical locations (y -coordinate) on the symmetry plane for $Ra = 10^6$ are plotted in Fig. 2(d). In addition to the good agreement between the solution profiles, we also plot the contours for the predicted temperature in Fig. 3 and the streamline contours in Fig. 4. The dimensionless heat transfer rate, which is defined as $Nu_{3D,v} = \int_0^1 Nu(z) dz$ where $Nu_{local}(x,y) = \frac{\partial T(y,z)}{\partial x}$ and $Nu(z) = \int_0^1 Nu_{local}(y,z) dy$, at the cold iso-thermal wall is represented by the Nusselt number. In the thermal driven cavity, we tabulate in Table 1 the predicted results for $u_{mp,max}(0,y,0)$ and $v_{mp,max}(x,0,0)$, where the subscript

“mp” denotes the mid-plane. These tabulated results are all seen to be in good agreement with the results of Haldenwang [33], Janssen et al. [34], Fikri [35], Henkes and Quéré [36], Tric et al. [37] and Haldenwang [33].

5. Results and discussion

As the control parameter Ra is increased, the dynamical system under current study becomes increasingly nonlinear and loses its

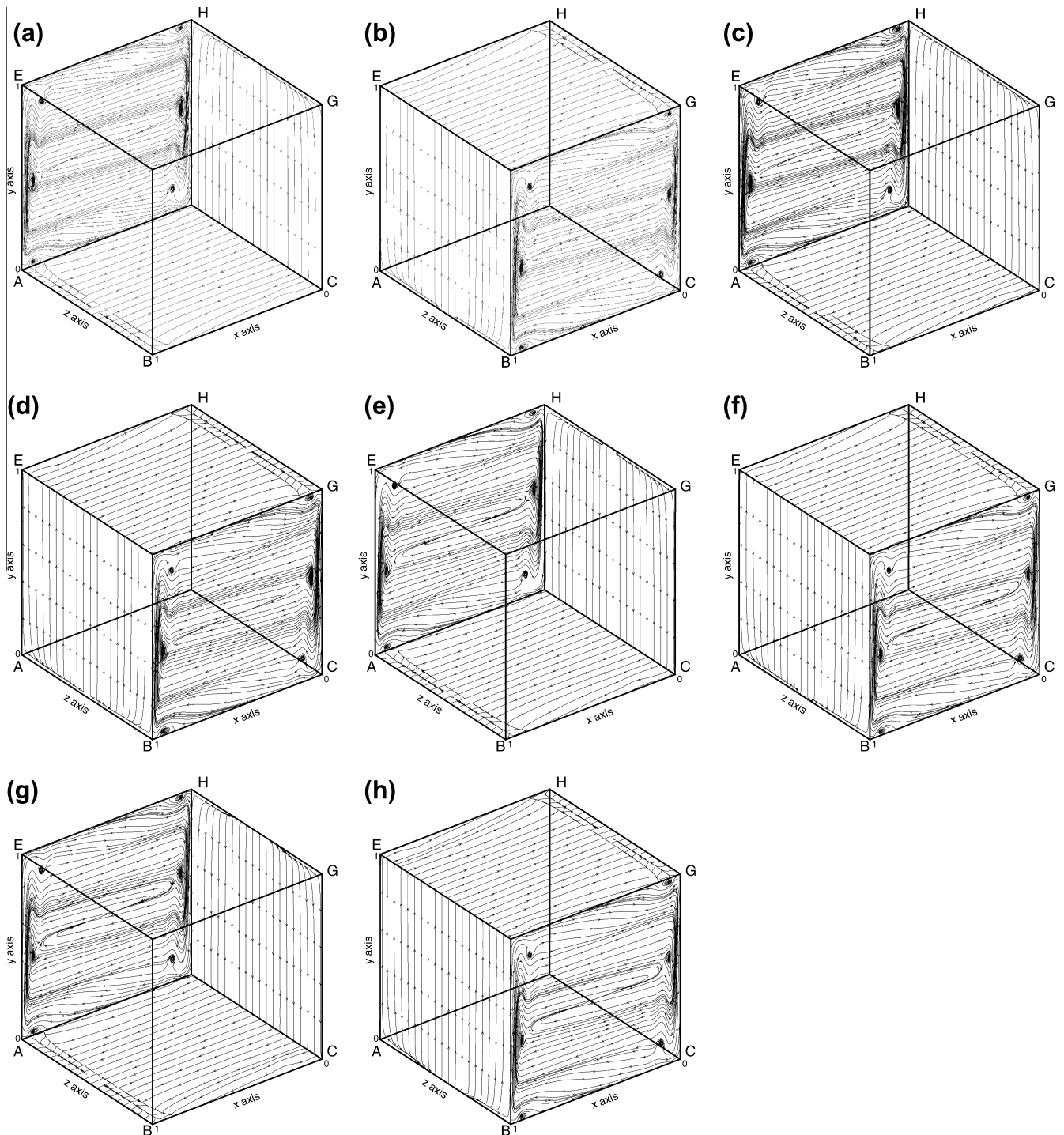


Fig. 14. The predicted limiting streamlines on the six cavity walls. (a) and (b) $Ra_P = 1.233 \times 10^8$; (c) and (d) $Ra_{FD_1} = 1.235 \times 10^8$; (e) and (f) $Ra_{FD_2} = 1.236 \times 10^8$; (g) and (h) $Ra_{FD_3} = 1.238 \times 10^8$.

stability. If one keeps increasing the value of Ra , the corresponding system will proceed towards chaos through three possible bifurcation routes, which are known as the periodic doubling route [38], quasi-periodic route [39] and intermittency route [40]. In the periodic doubling route, which is not found in the present study, the dynamic system loses its stability via period-doubling bifurcation and a number of accompanying subharmonics. In the quasi-periodic route to chaos, several subharmonic frequencies, which are irrationally related with the harmonic frequency, and several of its ultraharmonics and ultrasubharmonics will be exhibited. As for the intermittency route to chaos, which is also not found in the current study, the dynamic system is destabilized through intermittency. This implies that chaos appears intermittently within an otherwise regular trajectory.

Power spectrum analysis enables us to get the power versus frequency of the dynamical system using the currently simulated time-series solutions. Given a set of signals, which are either the

velocity components or the pressure, its power spectrum exhibits a portion of signal's power or energy per unit time falling within the given frequency bins. For a system proceeding towards chaos, more and more spectrum peaks, which have association with the harmonics, subharmonics, ultraharmonics and ultrasubharmonics [41], will be generated. Subharmonic frequencies can be expressed algebraically in terms of the fundamental (or driving, harmonic) frequency f_1 as [41]

$$f_i = \frac{1}{i} f_1 \tag{15}$$

where $i = 2, 4, 8, \dots$. As for the ultraharmonic and ultrasubharmonic frequencies, they can be expressed differently by the following expression

$$f_i = \frac{m}{n} f_1 \tag{16}$$

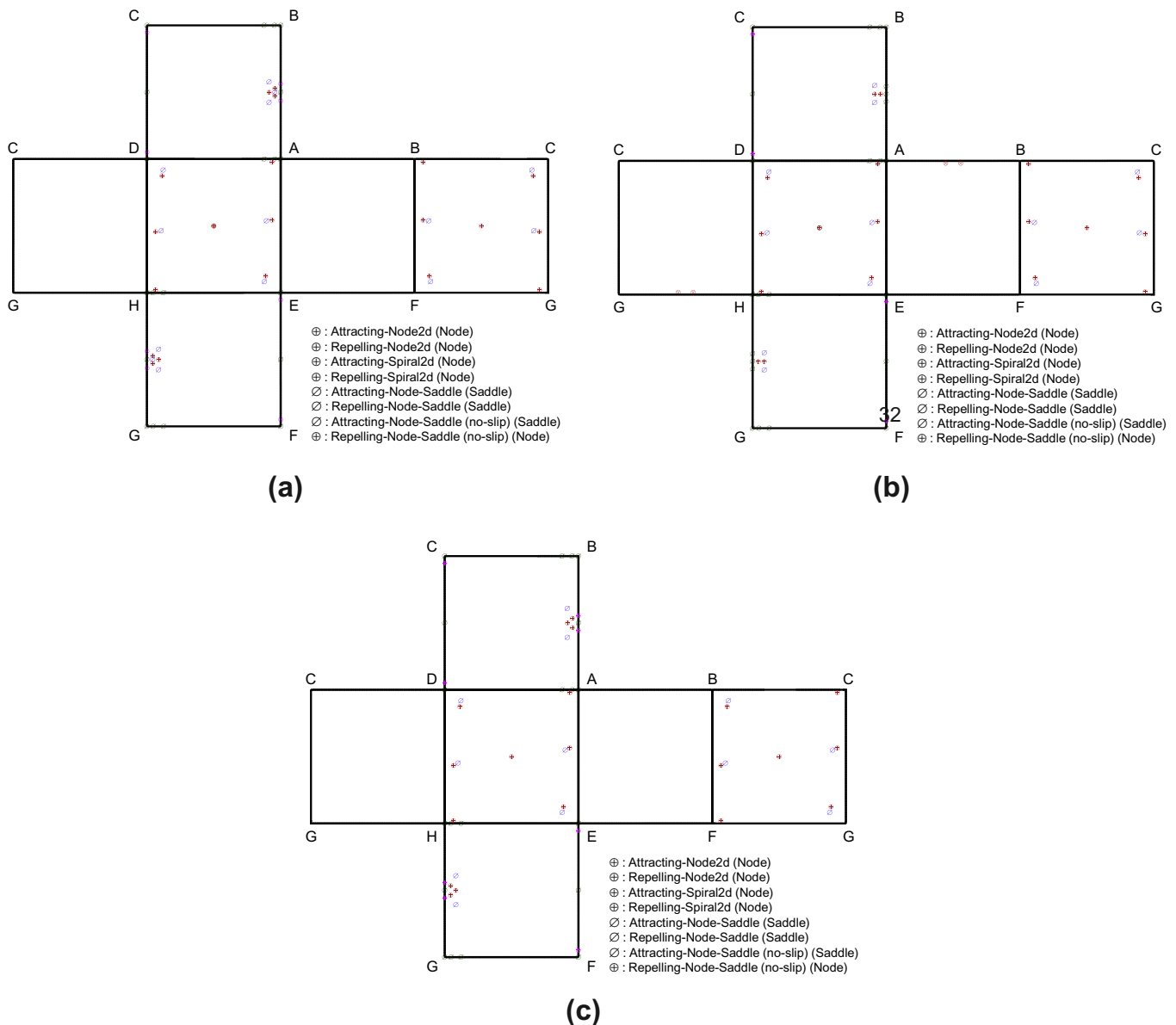


Fig. 15. Different topological classifications of the critical points on the six solid walls of the investigated thermal driven cavity. (a) $Ra_p = 1.233 \times 10^8$, where $N = 20, S = 14, N' = 8, S' = 20, (\sum N + \frac{1}{2} \sum N') - (\sum S + \frac{1}{2} \sum S') = 24 - 24 = 0$; (b) $Ra_{p1} = 1.235 \times 10^8$, where $N = 20, S = 14, N' = 8, S' = 20, (\sum N + \frac{1}{2} \sum N') - (\sum S + \frac{1}{2} \sum S') = 24 - 24 = 0$; (c) $Ra_{p2} = 1.236 \times 10^8$, where $N = 20, S = 14, N' = 8, S' = 20, (\sum N + \frac{1}{2} \sum N') - (\sum S + \frac{1}{2} \sum S') = 24 - 24 = 0$.

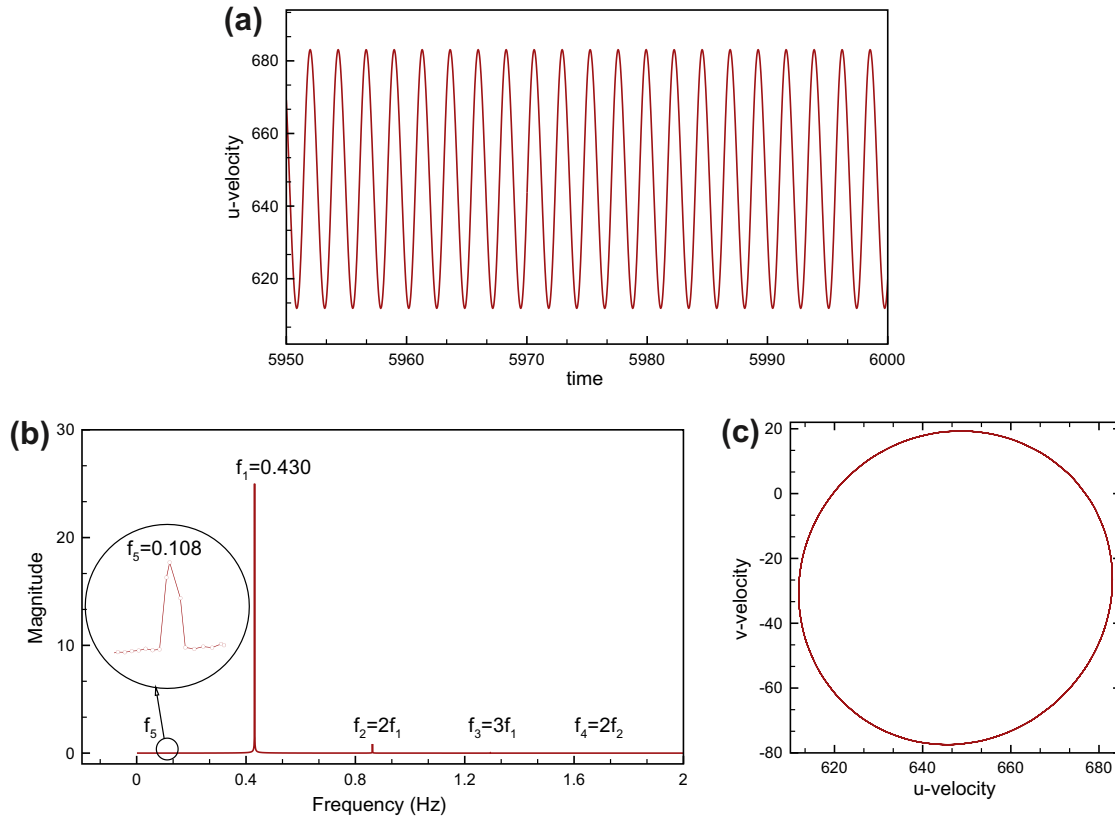


Fig. 16. The power spectrum of the u -velocity component predicted at the chosen point $(x,y,z) = (0.9, 0.9, 0.9)$, where $f_1 \approx 0.430$ Hz, $f_2 = 2f_1$, $f_3 = f_1 + f_2$, $f_4 = 2f_2$, $f_5 \approx 0.108$ Hz, for the case investigated at $Ra_{QP_1} = 1.278 \times 10^8$. (a) Time-evolving x -component velocity u ; (b) FFT plot; (c) limit cycle.

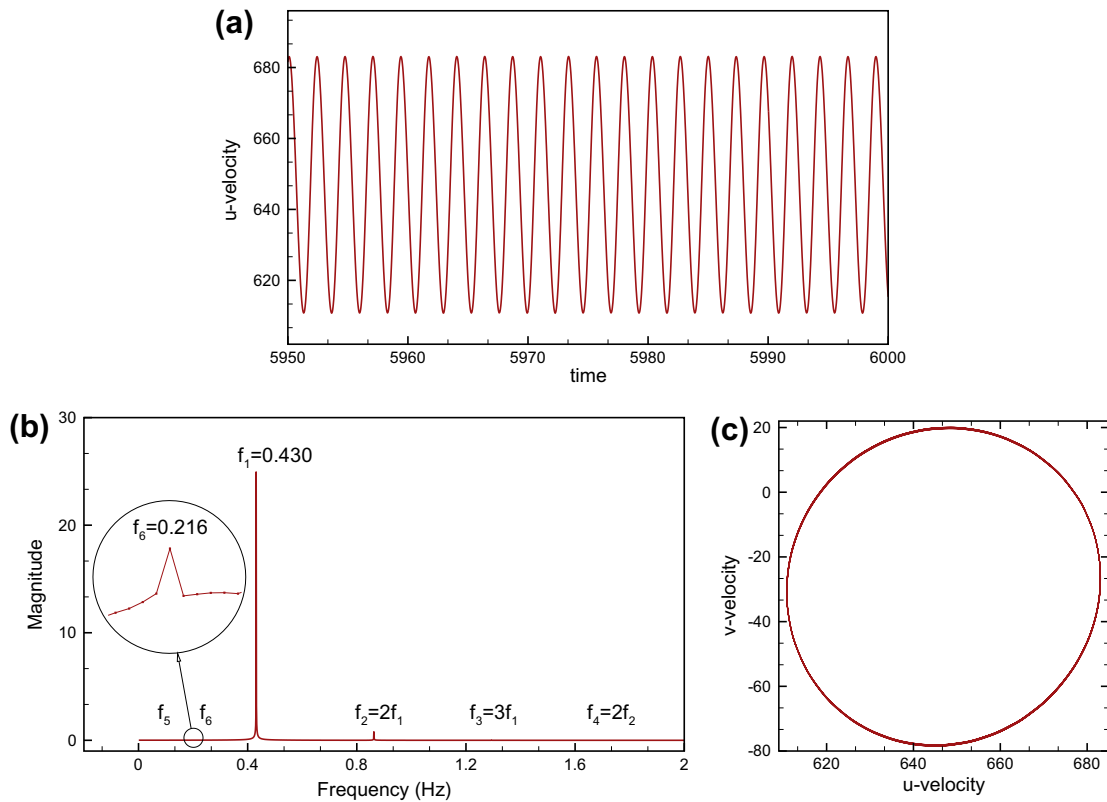


Fig. 17. The power spectrum of the u -velocity component predicted at the chosen point $(x,y,z) = (0.9, 0.9, 0.9)$, where $f_1 \approx 0.430$ Hz, $f_2 = 2f_1$, $f_3 = f_1 + f_2$, $f_4 = 2f_2$, $f_5 \approx 0.108$ Hz, $f_6 = 2f_5 \approx 0.216$ Hz, for the case investigated at $Ra_{QP_2} = 1.279 \times 10^8$. (a) Time-evolving x -component velocity u ; (b) FFT plot; (c) limit cycle.

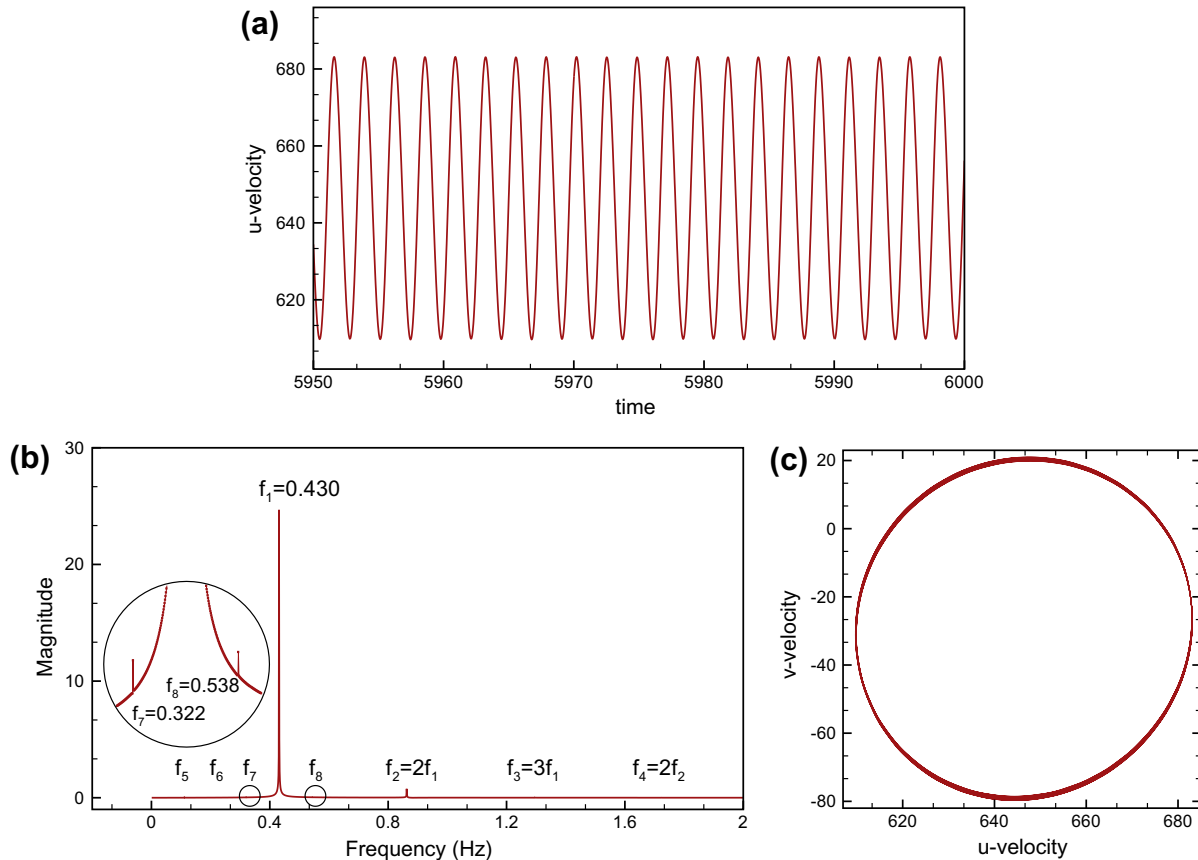


Fig. 18. The power spectrum of the u -velocity component predicted at the chosen point $(x, y, z) = (0.9, 0.9, 0.9)$, where $f_1 \approx 0.430$ Hz, $f_2 = 2f_1$, $f_3 = f_1 + f_2$, $f_4 = 2f_2$, $f_5 \approx 0.108$ Hz, $f_6 = 2f_5 \approx 0.216$ Hz, $f_7 = f_1 - f_5$ and $f_8 = f_1 + f_5$, for the case investigated at $Ra_{qp3} = 1.28 \times 10^8$. (a) Time-evolving x -component velocity u ; (b) FFT plot; (c) limit cycle.

Table 2
Summary of the three predicted families of bifurcations prior to chaos formation in the currently investigated nonlinear system.

Frequency no.	f_1	f_2	f_3	f_4	f_5	f_6	f_7	f_8
$Ra (\times 10^8)$	1.233	1.235	1.236	1.238	1.278	1.279	1.28	1.28
Frequencies (\approx)	0.430 (fundamental frequency)	$f_2 = 2f_1 \approx 0.860$	$f_3 = f_1 + f_2 \approx 1.290$	$f_4 = f_1 + f_3 \approx 1.720$	0.108	$f_5 = 2f_4 \approx 0.216$	$f_7 = f_1 - f_5 \approx 0.322$	$f_8 = f_1 + f_5 \approx 0.538$
Figure number	5	10	11	12	16	17	18	18
	Family-I (f_1 - f_4)				Family-II (f_5, f_6)		Family-III (f_7, f_8)	

where m and n are the two integers with $m > n$. As the truly chaotic state is approached, the system is featured to have a spectrum of frequencies rather than a finite number of specific peaks. Note that pitchfork bifurcation plays also an important role towards chaos. Due to space limitation, this type of bifurcation, which appears after Hopf bifurcation, will be discussed in the subsequent article.

5.1. Supercritical Hopf bifurcation and subharmonics

As the control parameter, which is the Rayleigh number Ra , of the presently investigated nonlinear system is beyond the predicted critical value of $Ra = 1.233 \times 10^8$, the original equilibrium flow submitted to a time independent forcing could no longer be steadily sustained. Such a flow destabilization gives birth to a limit cycle that is branched from the equilibrium state (or fixed point). In other words, the resulting Hopf bifurcation is accepted as the birth of limit cycle from an equilibrium state in dynamical system.

Hopf bifurcation can be supercritical or subcritical, leading either to a stable or an unstable limit cycle, respectively. The currently predicted supercritical Hopf bifurcation is orbitally stable due to the predicted negative first Lyapunov coefficient. In the subsequent discussion, our emphasis will be given to the numerically predicted limit cycles around the vortex cores.

Fig. 5 plots the predicted time-varying velocity component u (Fig. 5(a)) and its corresponding power spectrum (Fig. 5(b)) and phase portrait (Fig. 5(c)) at the critical value of Ra , which is 1.233×10^8 . Power spectrum plot depicts the portion of the simulated time-series solutions of the dynamical system, cast in terms of energy per unit time, falling in the frequency bins. The plot of phase portrait, which is a geometric representation of the trajectories of the current dynamical system in the phase plane, helps to clarify, for example, whether or not limit cycle will be present at the investigated value of Ra . The predicted power spectrum was featured solely with the harmonic frequency (or fundamental

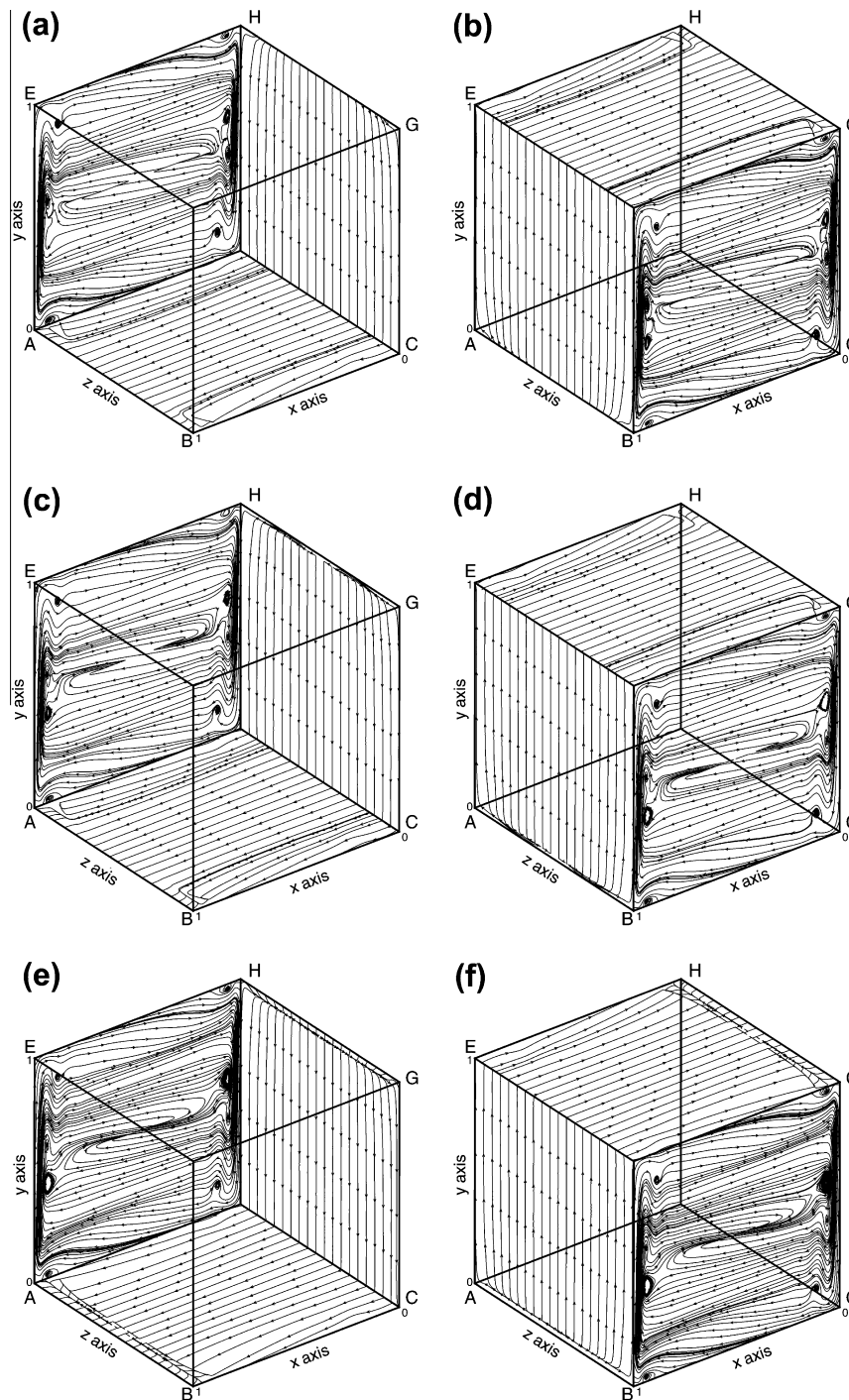


Fig. 19. The predicted limiting streamlines on the six cavity walls. (a, b) For $Ra_{QP_1} = 1.278 \times 10^8$; (c, d) for $Ra_{QP_2} = 1.279 \times 10^8$; (e, f) for $Ra_{QP_3} = 1.28 \times 10^8$.

frequency at $f_1 = 0.42998394$ Hz (≈ 0.430 Hz)). This frequency remains unchanged all the time but its driving amplitude becomes larger and larger with the increase of Rayleigh number. In Fig. 5(c), which plots the predicted periodic attractor or limit cycle, the fundamental frequency was seen accordingly in Fig. 5(b). It is observed that a solution point remained in the curve throughout the entire simulation. This implies that the solution point will be returned to its initial point periodically.

One proper way of depicting the vortical flow development due to the thermal buoyancy force established in the investigated cavity is to plot the predicted vortical corelines. Based on the velocity

components predicted at $Ra = 1.233 \times 10^8$, for example, we can get six major vortical corelines, marked by $VC_1, VC_2, VC_3, VC_1^*, VC_2^*$ and VC_3^* , and plot them in Fig. 6. These vortical corelines, emanated from their adjacent bounded wall surfaces, are separated into a group of vortical corelines (VC_1, VC_2, VC_3), which is symmetric to the other group of vortical corelines (VC_1^*, VC_2^*, VC_3^*) with respect to the plane (EFCD).

In regions adjacent to the vortical corelines, one can clearly find a complex spiral particle motion. Due to space limitation, we plot in Fig. 7 only for the particle trajectory along the vortical coreline VC_1 and leave the rest to be discussed in the next paper. On the line

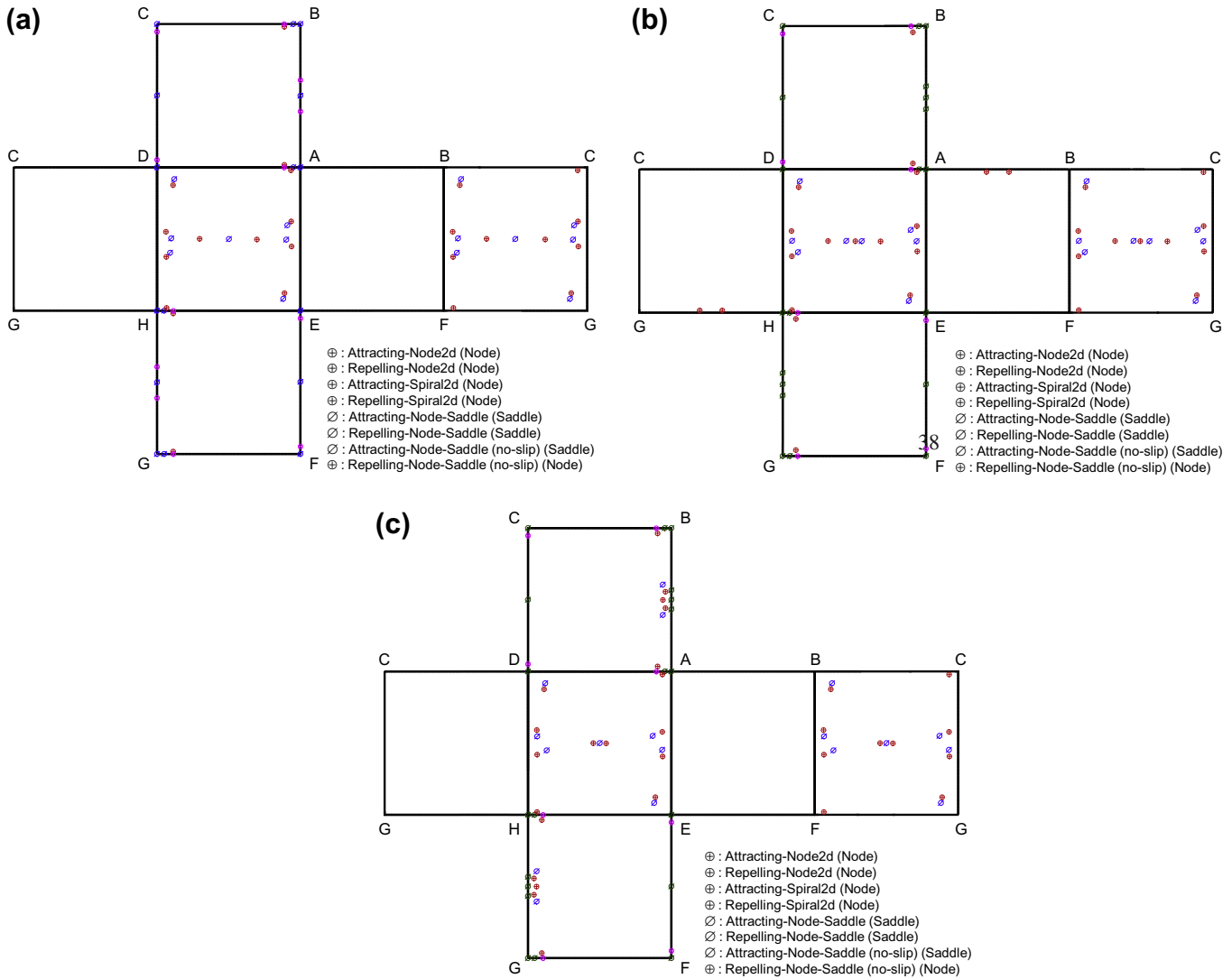


Fig. 20. Different topological classifications of the critical points on the six solid walls of the thermal driven cavity. (a) $Ra_{QP_1} = 1.278 \times 10^8$, where $N = 20, S = 14, N' = 8, S' = 20, (\sum N + \frac{1}{2} \sum N') - (\sum S + \frac{1}{2} \sum S') = 24 - 24 = 0$; (b) $Ra_{QP_2} = 1.279 \times 10^8$, where $N = 20, S = 14, N' = 8, S' = 20, (\sum N + \frac{1}{2} \sum N') - (\sum S + \frac{1}{2} \sum S') = 24 - 24 = 0$; (c) $Ra_{QP_3} = 1.28 \times 10^8$, where $N = 20, S = 14, N' = 8, S' = 20, (\sum N + \frac{1}{2} \sum N') - (\sum S + \frac{1}{2} \sum S') = 24 - 24 = 0$.

VC_1 , the velocity magnitude u_s that is locally tangential to line VC_1 is computed firstly and is then plotted in Fig. 8. It is surprisingly to find from Figs. 7 and 8 that both u_s and the spiral flow change sign and direction alternatingly. On the three chosen planes schematic in Fig. 8 that are approximately orthogonal to the line VC_1 , one can observe two different types of streamlines. These streamlines are seen to emanate from the vortical center and proceed outwards monotonically. There exists another set of streamlines with the particle trajectories moving outwards from the vortical center and one family of particle trajectories moving towards the vortical coreline from a region away from VC_1 . These two inward–outward moving particle trajectories meet each other at the so-called limit cycle shown in Fig. 9. In other words, the predicted limit cycle divides the vortical flow into an inner unstable vortex flow with its direction moving away from the vortex coreline and an outer stable vortex flow with the direction pointing towards the vortex coreline.

As Ra is increased to a value slightly larger than 1.233×10^8 , the harmonic frequency remains unchanged but a stable periodic orbit is gradually evolved to form a slightly modified periodic orbit, shown in Fig. 10(b), having the frequency that is two times

of its fundamental frequency f_1 (or $f_2 = 2f_1 = 0.85996789$ Hz (≈ 0.860 Hz)) at $Ra_{FD_1} = 1.235 \times 10^8$. If the Rayleigh number is increased further to $Ra_{FD_2} = 1.236 \times 10^8$, the third dominant frequency, namely, $f_3 = f_1 + f_2 = 1.289951289$ Hz (≈ 1.290 Hz), which is commensurate with f_1 and f_2 , was observed in Fig. 11(b). Another frequency doubling bifurcation, with respect to frequency f_2 , was observed at $Ra_{FD_3} = 1.238 \times 10^8$ with the frequency $f_4 = 2f_2 = 4f_1 = 1.7209630$ Hz (≈ 1.720 Hz) shown in Fig. 12(b). Note that frequency f_4 is also commensurate with f_1 and f_3 in the sense that $f_4 = f_1 + f_3$. Contradictory to the bifurcation that leading to doubling period, which is known as one of the three routes to chaos, the currently predicted period-halving bifurcation still puts the system into order. Frequencies f_2, f_3 and f_4 are referred to as ultraharmonics and ultrasubharmonics [41]. Fig. 13 summarizes the predicted periodic solutions, plotted together with the limit cycles, based on the phase portraits in the bifurcation range I, which is $1.233 \times 10^8 \leq Ra \leq 1.238 \times 10^8$. For completeness, we plot the limiting streamlines at the six walls in Fig. 14 and the predicted critical points in Fig. 15 for the flows investigated at $Ra = 1.233 \times 10^8, 1.235 \times 10^8, 1.236 \times 10^8$ and 1.238×10^8 .

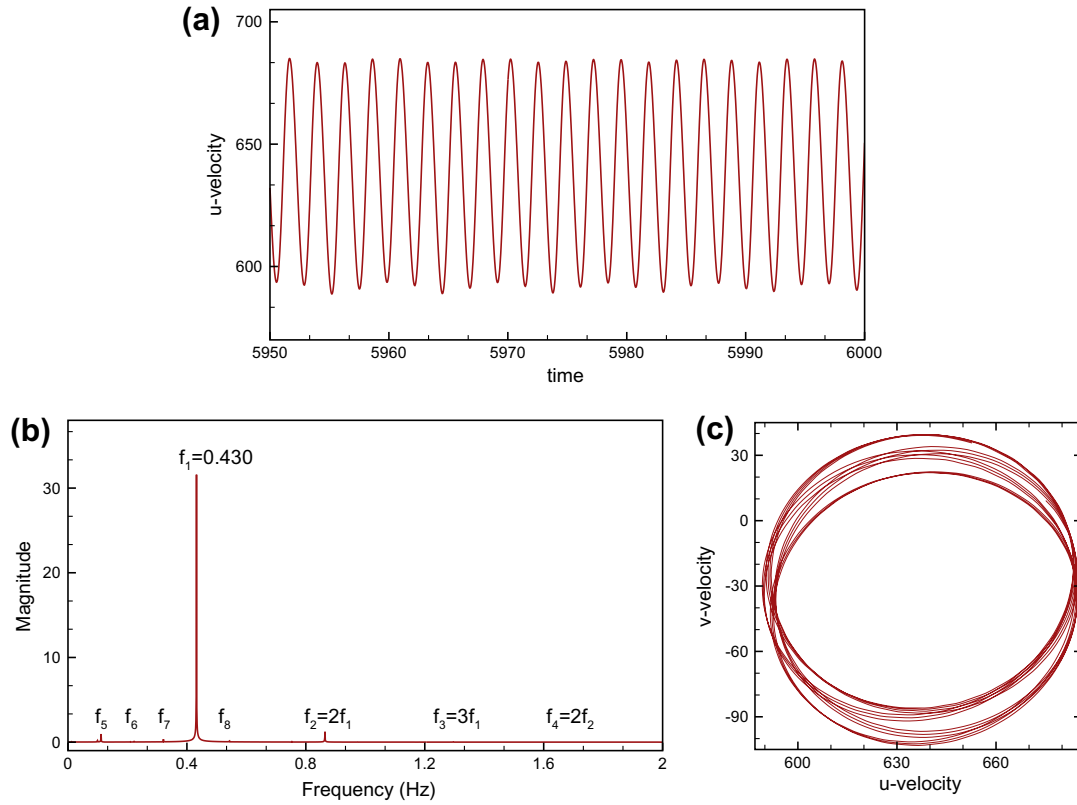


Fig. 21. The power spectrum of the u -velocity component predicted at the chosen point $(x,y,z) = (0.9,0.9,0.9)$, where $f_1 \approx 0.430$ Hz, $f_2 = 2f_1$, $f_3 = f_1 + f_2$, $f_4 = 2f_2$, $f_5 \approx 0.108$ Hz, $f_6 = 2f_5 \approx 0.216$ Hz, $f_7 = f_1 - f_5$ and $f_8 = f_1 + f_5$, for the case investigated at $Ra_{QP_4} = 1.3 \times 10^8$. (a) Time-evolving x -component velocity u ; (b) FFT plot; (c) limit cycle.

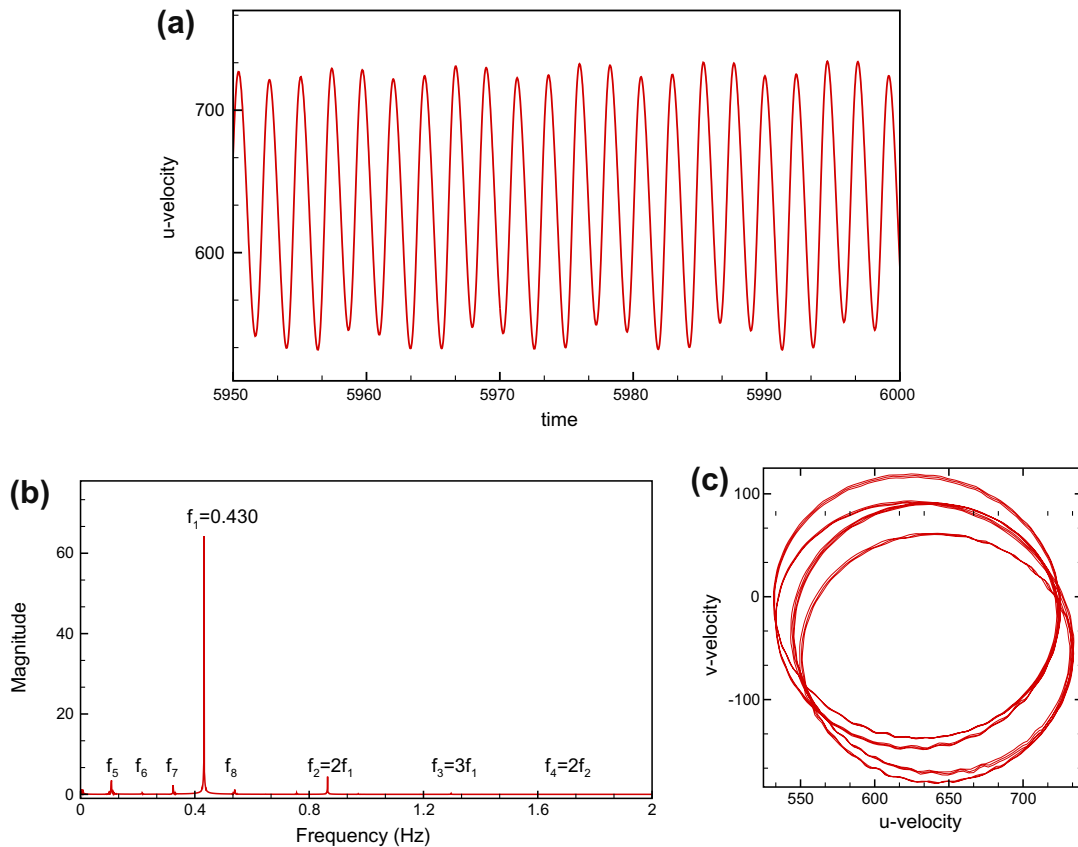


Fig. 22. The power spectrum of the predicted u -velocity component at the chosen point $(x,y,z) = (0.9,0.9,0.9)$, where $f_1 \approx 0.430$ Hz, $f_2 = 2f_1$, $f_3 = f_1 + f_2$, $f_4 = 2f_2$, $f_5 \approx 0.108$ Hz, $f_6 = 2f_5 \approx 0.216$ Hz, $f_7 = f_1 - f_5$ and $f_8 = f_1 + f_5$, for the case investigated at $Ra = 1.5 \times 10^8$. (a) Time-evolving x -component velocity u ; (b) FFT plot; (c) limit cycle.

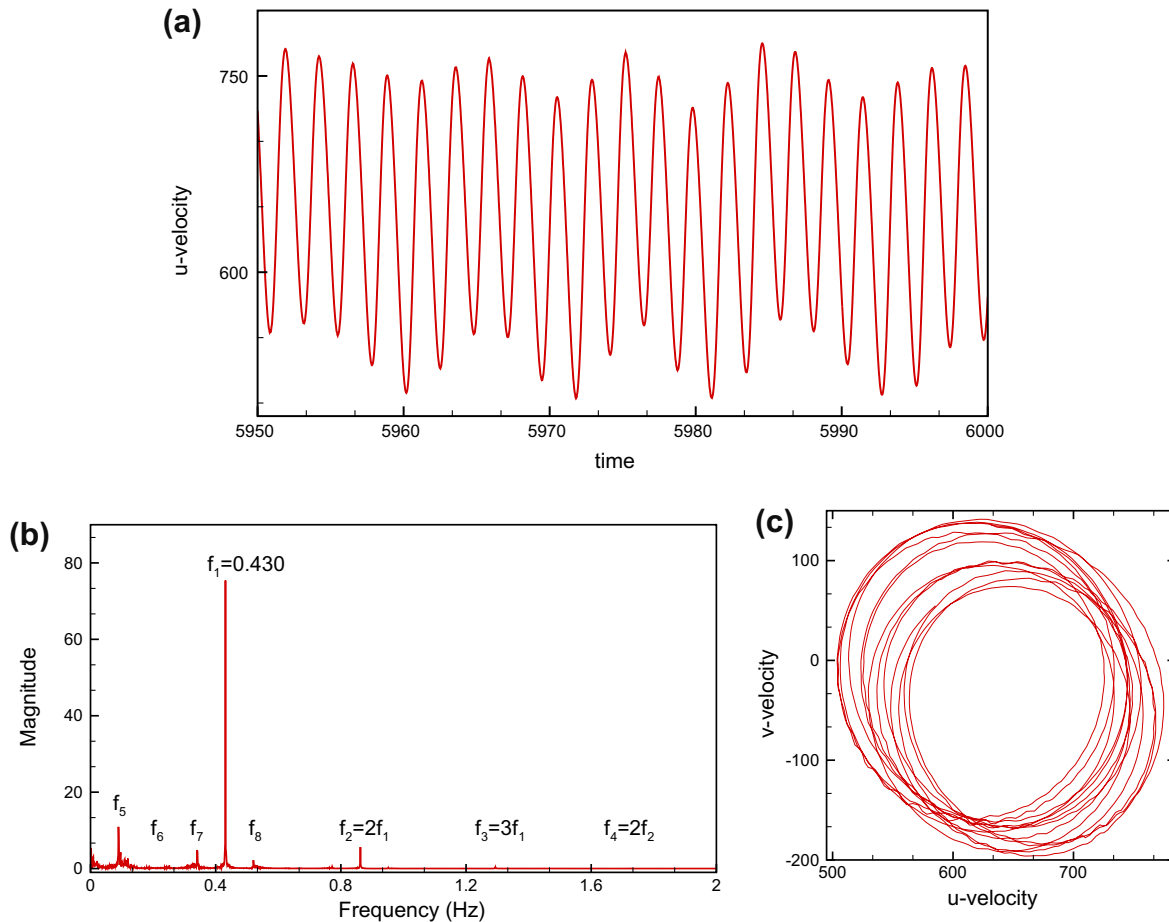


Fig. 23. The power spectrum of the predicted u -velocity component at the chosen point $(x, y, z) = (0.9, 0.9, 0.9)$, where $f_1 \approx 0.430$ Hz, $f_2 = 2f_1$, $f_3 = f_1 + f_2$, $f_4 = 2f_2$, $f_5 \approx 0.108$ Hz, $f_6 = 2f_5 \approx 0.216$ Hz, $f_7 = f_1 - f_5$ and $f_8 = f_1 + f_5$, for the case investigated at $Ra = 1.6 \times 10^8$. (a) Time-evolving x -component velocity u ; (b) FFT plot; (c) limit cycle.

5.2. Quasi-periodic bifurcation

As the value of Ra was increased to 1.278×10^8 , a new bifurcation type (or bifurcation II) featured with the frequency $f_5 = 0.10836993$ Hz (≈ 0.108 Hz) is predicted and plotted in Fig. 16. We are followed by plotting its ultraharmonic mode $f_6 = 2f_5 = 0.21673986$ Hz (≈ 0.216 Hz) in Fig. 17 at $Ra_{QP_2} = 1.279 \times 10^8$. This predicted subharmonic frequency f_5 is incommensurate with the harmonic frequency f_1 and all other previously predicted family-I frequencies.

Subharmonic frequency denotes the frequency below the fundamental frequency of an oscillator and can be expressed by f_1/m , where $m = 1, 2, 4, 8, \dots$ [41]. In the recognition of these two predicted periodic orbits containing the irrationally related frequencies, we are led to know the initiation of a quasi-periodic bifurcation. Note that such a quasi-periodic route has been known as one of the three major routes to chaos. In other words, the existence of quasi-periodic bifurcation hints the presence of another precursor for a flow possibly evolving to chaos. This bifurcation type is quite a common route to chaos. After the stable fixed point turning into a limit cycle via Hopf bifurcation, this limit cycle may proceed through a second Hopf bifurcation and is then developed into a two-frequency torus or even a three-torus via another Hopf bifurcation provided that the nonlinear control parameter keeps increasing and, finally, the investigated flow may develop into turmoil.

The second frequency-doubling bifurcation, shown in Fig. 17, was observed as Ra was increased to 1.279×10^8 . Except the two predicted families of bifurcations with the frequencies f_1 and f_5 ,

two other modal frequencies with $f_7 = f_1 - f_5 = 0.32164010$ Hz (≈ 0.322 Hz) and $f_8 = f_1 + f_5 = 0.53835387$ Hz (≈ 0.538 Hz, $Ra_{QP_3} = 1.28 \times 10^8$) made their appearance and they are shown in Fig. 18. While some additional visible frequencies may appear in the power spectrum prior to the chaotic flow, their amplitudes were however several orders smaller than the amplitude of the primary frequency f_1 . In conclusion, the predicted bifurcation route prior to chaos is tabulated in Table 2. As before, we also plot the predicted limiting streamlines on the six walls in Fig. 19 together with their critical points in Fig. 20 for the flow investigated at $Ra = 1.278 \times 10^8$, 1.279×10^8 and 1.28×10^8 for the sake of completeness.

5.3. Transition to chaos

After the period-halving bifurcation, where the system has undergone two ultraharmonic bifurcations, and the quasi-periodic bifurcation route, which involves a number of periodic solutions with some irrationally related frequencies, the subsequent bifurcations are marked with an increasingly shorter and shorter Rayleigh number interval. Eventually, an infinite number of frequencies without any specific peak will be observed. At this moment, chaos was set in at a Rayleigh number that is larger than 1.3×10^8 . The process that the solutions evolve firstly from the fixed point to the periodic attractor and then to the two-torus limit set constitutes the route to chaos.

Transition from the periodic to chaotic regime is a rapid and complex process. Figs. 21–25 show the predicted time-series solutions, power spectra, and the corresponding phase portraits,

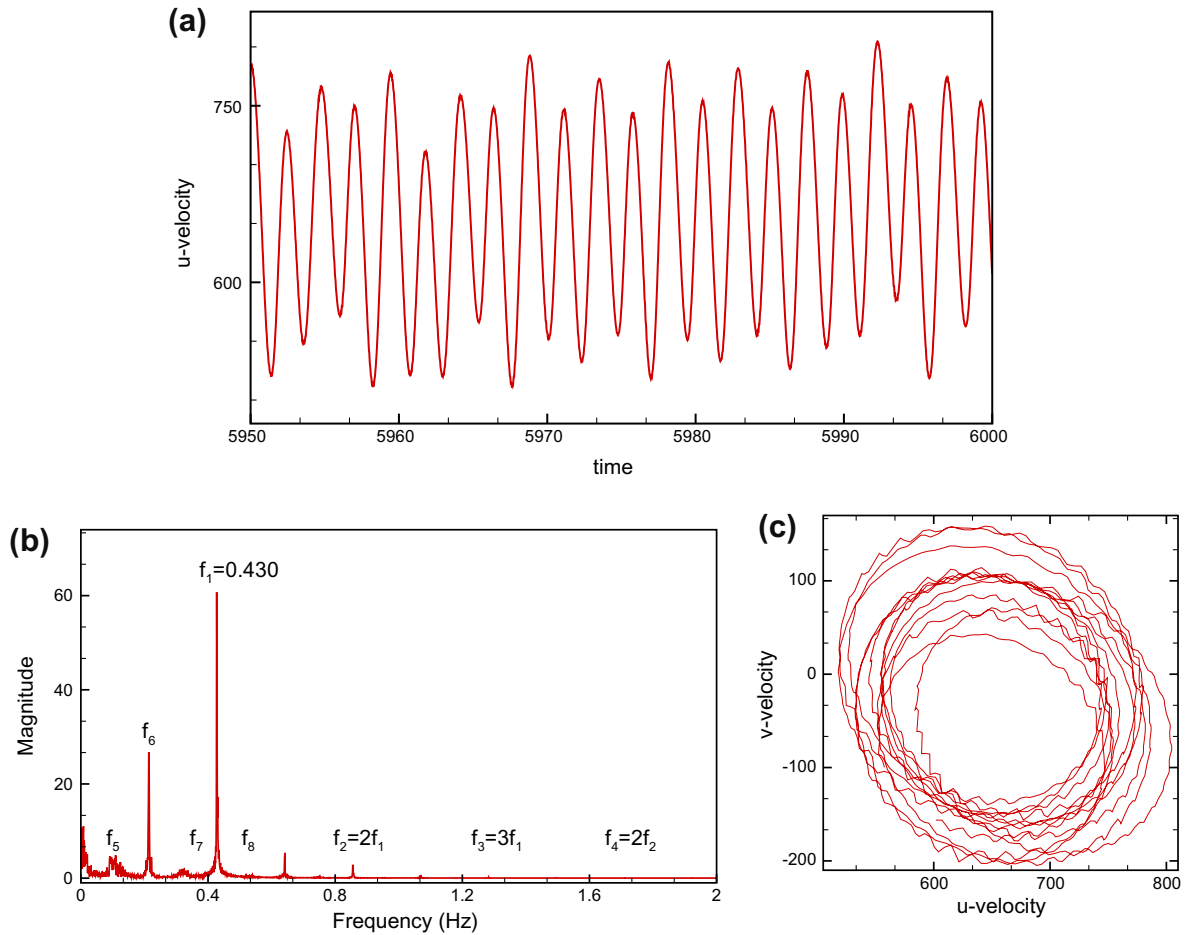


Fig. 24. The power spectrum of the predicted u -velocity component at the chosen point $(x, y, z) = (0.9, 0.9, 0.9)$, where $f_1 \approx 0.430$ Hz, $f_2 = 2f_1$, $f_3 = f_1 + f_2$, $f_4 = 2f_2$, $f_5 \approx 0.108$ Hz, $f_6 = 2f_5 \approx 0.216$ Hz, $f_7 = f_1 - f_5$ and $f_8 = f_1 + f_5$, for the case investigated at $Ra = 1.8 \times 10^8$. (a) Time-evolving x -component velocity u ; (b) FFT plot; (c) limit cycle.

respectively, in the range of $1.3 \times 10^8 \leq Ra \leq 2 \times 10^8$. The simulated time-series solutions in these figures show that the two central frequencies and peaks other than those of the frequencies $f_2 \sim f_4$ and $f_6 \sim f_8$ are not algebraically related.

The number of critical points of different types, which satisfy the topological rules of Hunt et al. [42] and Lighthill [43], predicted at the critical values of Ra are also tabulated in Table 3 as an additional confirmation of the physically plausible prediction performed in the current study. The bifurcation route to chaos in the currently investigated thermal driven cavity can be summarized as follows: Equilibrium or steady-state (S) \rightarrow periodic (P) \rightarrow frequency-doubling with ultraharmonics or ultrasubharmonics ($FD_1 \rightarrow FD_2 \rightarrow FD_3$) \rightarrow quasi-periodic ($QP_1 \rightarrow QP_2 \rightarrow QP_3$) \rightarrow chaotic (C). In a nutshell, Table 4 summarizes the Ra values and the corresponding number of frequencies along with their figure numbers from the periodic bifurcation to the chaotic bifurcation.

6. Conclusions

The present study is aimed to confirm the developed three-dimensional flow bifurcation scenario in the buoyancy-driven nonlinear system by employing a computationally stable and accurate scheme, which minimizes the dispersion error in flow conditions when convection dominates diffusion. Our aim is to explore complex flow behaviors, including the co-existing periodic (harmonic, subharmonic, ultraharmonic, and ultrasubharmonic) and aperiodic (quasi-periodic and chaotic) solutions, in the thermally driven flow

field. The conclusions drawn from this study are summarized below. At a Rayleigh number that is smaller than $Ra = 1.233 \times 10^8$, the predicted solution converges to a fixed (or steady-state) solution. As the Rayleigh number becomes slightly larger than the critical value, which is 1.233×10^8 , the investigated system becomes destabilized through Hopf bifurcation and the steady-state flow can no longer be sustained. The predicted stable supercritical Hopf bifurcation solution is featured with the formation of limit cycle. As the Rayleigh number is increased by a small amount to the value, for example, $Ra_{FD_1} = 1.235 \times 10^8$, the periodic solution featured with the harmonic frequency f_1 ($=0.430$ Hz) and driving magnitude is evolved to add one additional ultraharmonic frequency f_2 , whose magnitude ($=0.860$ Hz) exactly doubles the fundamental frequency. The resulting periodic solution is called the frequency-doubling (or period-halving) solution. The third frequency, which is exactly the sum of f_1 and f_2 , and the fourth frequency, which doubles the frequency f_2 , become to make their appearance in the simulated solutions for the case investigated at $Ra_{FD_2} = 1.236 \times 10^8$. We classify the solutions predicted at a Rayleigh number between 1.233×10^8 and 1.238×10^8 as the family-I solution in the sense that their ultraharmonic frequencies have close relevance to the fundamental (or harmonic) frequency f_1 . As the Rayleigh number keeps increasing to $Ra_{QP_1} = 1.278 \times 10^8$, a new frequency which is incommensurate with the family-I frequencies is predicted. The appearance of frequency f_5 in the predicted power spectrum suggests that the investigated flow system has evolved to the quasi-periodic bifurcation state. Like the two frequency-doubling solutions observed in the family-I periodic

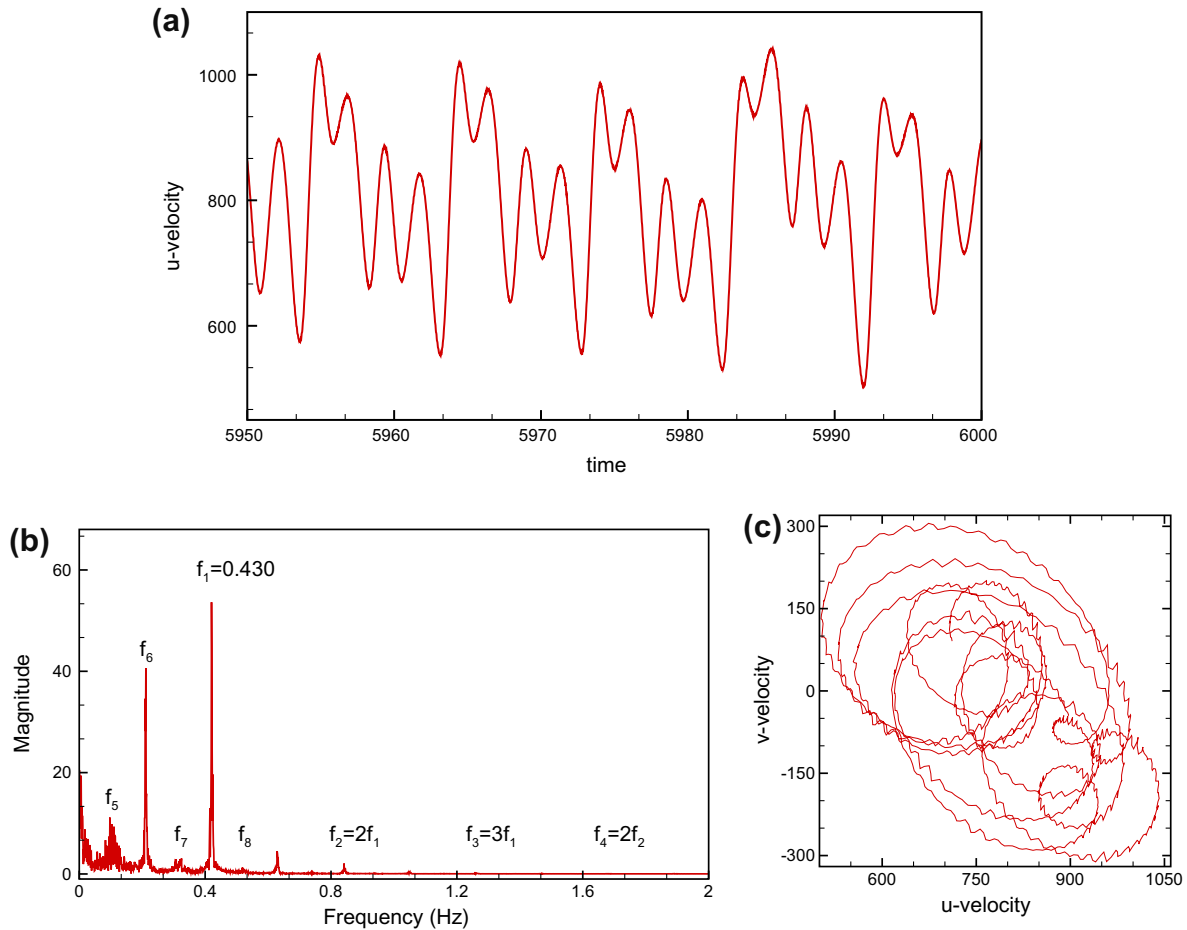


Fig. 25. The power spectrum of the predicted u -velocity component at the chosen point $(x, y, z) = (0.9, 0.9, 0.9)$, where $f_1 \approx 0.430$ Hz, $f_2 = 2f_1$, $f_3 = f_1 + f_2$, $f_4 = 2f_2$, $f_5 \approx 0.108$ Hz, $f_6 = 2f_5 \approx 0.216$ Hz, $f_7 = f_1 - f_5$ and $f_8 = f_1 + f_5$, for the case investigated at $Ra = 2 \times 10^8$. (a) Time-evolving x -component velocity u ; (b) FFT plot; (c) limit cycle.

Table 3
The number of critical points of different topological types predicted at different critical values of Ra in the presently investigated nonlinear system.

Ra	Attracting-Node2d (N)	Attracting-Spiral2d (N)	Repelling-Node2d (N)	Repelling-Spiral2d (N)	On-multiple-no-slip (S')	On-multiple-no-slip (N')	Saddle (S)	Saddle (S)	
1.23×10^8	4	4	4	8	20	8	6	8	62
1.231×10^8	4	4	4	8	20	8	6	8	62
1.232×10^8	4	4	4	8	20	8	6	8	62
1.233×10^8	6	4	4	8	20	8	6	8	64
1.234×10^8	5	4	4	8	20	8	6	8	63
1.235×10^8	6	4	6	8	24	4	4	8	64
1.236×10^8	4	4	4	8	20	8	6	8	62
1.237×10^8	4	4	4	8	20	8	6	8	62
1.238×10^8	5	8	4	8	20	8	6	12	71
1.239×10^8	6	4	8	8	24	4	8	8	70
1.24×10^8	5	8	4	8	20	8	6	12	71
1.25×10^8	4	4	4	8	20	8	6	8	62
1.26×10^8	2	4	4	8	20	8	6	8	60
1.27×10^8	4	4	8	8	24	4	8	8	68
1.276×10^8	12	8	0	8	16	12	4	14	74
1.277×10^8	4	4	6	8	24	4	6	8	64
1.278×10^8	8	8	0	8	16	12	4	10	66
1.279×10^8	10	12	4	4	20	8	4	12	74
1.28×10^8	10	8	6	8	20	8	6	14	80
1.281×10^8	4	12	0	8	18	14	4	18	78

solutions, the third frequency-doubling solution with the frequency f_6 ($Ra_{QP1} = 1.278 \times 10^8$) is also predicted. To distinguish the family-I periodic solutions, which include the frequencies $f_1, f_2,$

f_3 and f_4 , from other predicted solutions, we will designate the solutions with the frequencies f_5 and f_6 as the family-II periodic solutions. A slight increase of Ra to 1.28×10^8 , the solutions

Table 4

The simulated route to chaos in the presently investigated nonlinear system.

Route to chaos	Steady (S) → periodic (P) →	Periodic (FD ₁) →	Periodic (FD ₂) →	Periodic (FD ₃) →	Quasi periodic (QP ₁) →	Quasi Periodic (QP ₂) →	Quasi periodic (QP ₃) →	Chaotic (C)
<i>Ra</i>	1.233×10^8	1.235×10^8	1.236×10^8	1.238×10^8	1.278×10^8	1.279×10^8	1.28×10^8	1.5×10^8
Number of peak frequencies	1	2	3	4	4	5	8	–
Figure number	5	10	11	12	16	17	18	25

belonging to family-I and -II start to interact with each other and yield the solutions with two newly observed frequencies f_7 and f_8 . It is interesting to find from this study that f_7 and f_8 are nothing but the subtraction and the summation of the frequencies f_1 and f_5 , respectively. The solutions with the frequencies f_7 and f_8 are denoted as the family-III solutions in the presently investigated nonlinear system. After evolving one of the three major routes to chaos, which is the quasi-periodic bifurcation route, a slight increase of the value *Ra* to 1.28×10^8 causes the flow to bifurcate furthermore by exhibiting a much more complicated power spectrum. More and more rapidly evolving frequencies are observed and the flow finally becomes chaotic at $Ra = 1.5 \times 10^8$.

Acknowledgements

The financial supports provided by the National Science Council under Grants NSC97-2221-E-002-250-MY3 and CQSE project 97R0066-69 are gratefully acknowledged. Computational hardware supports from the National Center of High-performance Computing (NCHC) and the Computer Center of National Taiwan University are also highly appreciated.

References

- [1] P. Sonda, A. Yeckel, P. Daoutidis, J.J. Derby, Hopf bifurcation and solution multiplicity in a model for destabilized Bridgman crystal growth, *Chem. Eng. Sci.* 60 (2005) 1323–1336.
- [2] C. Chang, R. Brown, Natural convection in steady solidification: finite element analysis of a two-phase Rayleigh–Bénard problem in a cavity, *J. Comput. Phys.* 53 (1984) 1–26.
- [3] J. Baumgartl, W. Budweiser, G. Muller, G. Neumann, Studies of buoyancy driven convection in vertical cylinder with parabolic temperature profile, *J. Cryst. Growth* 97 (1989) 9–17.
- [4] B. Roux, H. Hadid, P. Laure, Numerical simulation of oscillatory convection in semiconductor melts, *J. Cryst. Growth* 97 (1989) 201–216.
- [5] H. Hadid, B. Roux, Buoyancy-and thermocapillary-driven flows in a shallow open cavity: unsteady flow regimes, *J. Cryst. Growth* 97 (1989) 217–225.
- [6] C. Le Marec, R. Guerin, P. Haidenwang, Pattern study in the 2-D solutal convection above a Bridgman-type solidification front, *Phys. Fluids* 9 (1997) 3149–3161.
- [7] C. Lan, D. Yang, Dynamic simulation of the vertical zone-melting crystal growth, *Int. J. Numer. Methods Heat Fluid Flow* 41 (1998) 4351–4373.
- [8] Y. Yamaguchi, C. Chang, R. Brown, Multiple buoyancy driven flows in a vertical cylinder heated from below, *Philos. Trans. Roy. Soc. London* 312 (1984) 519–552.
- [9] D.J. Ma, D.J. Sun, X.Y. Yin, Multiplicity of steady states in cylindrical Rayleigh–Bénard convection, *Phys. Rev. E* 74 (037302) (2006) 1–4.
- [10] A.Y. Gelfgat, P.Z. Bar-Yoseph, A.L. Yarin, Stability of multiple steady states of convection in laterally heated cavities, *J. Fluid Mech.* 388 (1999) 315–334.
- [11] J.P. Pulicani, E. Crespo del Arco, A. Randriamampianina, P. Bontoux, R. Peyret, Spectral simulations of oscillatory convection at low Prandtl number, *Int. J. Numer. Methods Fluids* 10 (1990) 481–517.
- [12] R. Bennacer, M. El Ganaoui, E. Leonardi, Vertical Bridgman configuration heated from below: 3-D bifurcation and stability analysis, in: *Third International Conference on CFD in the Minerals and Process Industries CSIRO, Australia*, 2003.
- [13] H. Yahata, Stability analysis of natural convection in vertical cavities with lateral heating, *J. Phys. Soc. Jpn.* 68 (2) (1999) 446–460.
- [14] J.W. Elder, Laminar free convection in a vertical slot, *J. Fluid Mech.* 23 (1965) 77–98.
- [15] N. Seki, S. Fukusako, H. Inaba, Visual observation of natural convective flow in a narrow vertical cavity, *J. Fluid Mech.* 84 (1978) 695–704.
- [16] J. Guckenheimer, P. Holmes, *Nonlinear Oscillations, Dynamical Systems, and Bifurcations of Vector Fields*, Applied Mathematical Science, vol. 42, Springer-Verlag, New York, 1983.
- [17] S. Wiggins, *Introduction to Applied Nonlinear Dynamical Systems and Chaos*, Texts in Applied Mathematics, vol. 2, Springer-Verlag, New York, 1990.
- [18] E.J.N. Ketchamen, L. Nana, T.C. Kofane, Strange nonchaotic attractors in the externally modulated Rayleigh–Bénard system, *Chaos Solitons Fract.* (CS&F) 20 (2004) 1141–1148.
- [19] E.H. Abed, P.P. Varaiya, Nonlinear oscillations in power systems, *Int. J. Elec. Power Eng. Syst.* 6 (1) (1984) 37–43.
- [20] V. Ajjarapu, B. Lee, Bifurcation theory and its application to nonlinear dynamical phenomena in an electrical power system, *IEEE Trans. Power Syst.* 7 (1) (1992) 424–431.
- [21] P. Le Quere, M. Behnia, From onset of unsteadiness to chaos in a differentially heated square cavity, *J. Fluid Mech.* 359 (1998) 81–107.
- [22] S. Xin, P. Le Quere, Linear stability analyses of natural convection in a differentially heated square cavity with conducting horizontal walls, *Phys. Fluids* 13 (9) (2001) 2529–2542.
- [23] G.E. Lixin, C.A.I. Qingdong, The topology of the sectional streamlines, *Commun. Nonlinear Sci. Numer. Simulat.* 3 (4) (1998) 203–206.
- [24] H. Hakin, *Instability Hierarchies of Self Organizing Systems and Devices in Advanced Synergetics*, Springer-Verlag, Berlin, 1984.
- [25] P. Grassberger, I. Procaccia, Characterization of strange attractors, *Phys. Rev. Lett.* 50 (1983) 346–349.
- [26] O.A. Ladyzhenskaya, *The Mathematical Theory of Viscous Incompressible Flow*, Gordon & Breach, New York, 1969.
- [27] T.W.H. Sheu, P.H. Chiu, A divergence-free-condition compensated method for incompressible Navier–Stokes equations, *Comput. Methods Appl. Mech. Eng.* 196 (2007) 4479–4494.
- [28] P.H. Chiu, T.W.H. Sheu, R.K. Lin, Development of a dispersion-relation-preserving upwinding scheme for incompressible Navier–Stokes equations on non-staggered grids, *Numer. Heat Transfer, B Fundamentals* 48 (2005) 543–569.
- [29] C. Bogry, C. Bailly, A family of low dispersive and low dissipative explicit schemes for flow and noise computations, *J. Comput. Phys.* 194 (2004) 194–214.
- [30] C.K.W. Tam, J.C. Webb, Dispersion-relation-preserving finite difference schemes for computational acoustics, *J. Comput. Phys.* 107 (1993) 262–281.
- [31] I.A. Abalakin, A.V. Alexandrov, V.G. Bobkov, T.K. Kozubskaya, High accuracy methods and software development in computational aeroacoustics, *J. Comput. Methods Sci. Eng. (JCMSE)* 2 (3) (2003) 1–14.
- [32] K.L. Wong, A.J. Baker, A 3D incompressible Navier–Stokes velocity–vorticity weak form finite element algorithm, *Int. J. Numer. Methods Fluids* 38 (2002) 99–123.
- [33] P. Haldenwang, Résolution Tridimensionnelle Deséquations de Navier–Stokes par Méthodes Spectrales Tchebycheff: Application à la Convection Naturelle, Thèse d’Etat, Université de Provence, 1984.
- [34] R.J.A. Janssen, R.A.W.M. Henkes, C.J. Hoogendoorn, Transition to time-periodicity of a natural-convection flow in a 3D differentially heated cavity, *Int. J. Heat Mass Transfer* 36 (1993) 2927–2940.
- [35] A. Fikri, Simulation Numérique 3D, en Collocation Chebyshev, de PheAnomènes Thermoconvectifs en Centrifugation, Thèse de l’Université Paris-Sud XI, Orsay, 1993.
- [36] R.A.W.M. Henkes, P. Le Quéré, Three-dimensional transition of natural-convection flows, *J. Fluid Mech.* 319 (1996) 281–303.
- [37] E. Tric, G. Labrosse, M. Betrouni, A first incursion into the 3D structure of natural convection of air in a differentially heated cubic cavity, from accurate numerical solutions, *Int. J. Heat Mass Transfer* 43 (2000) 4043–4056.
- [38] M.J. Feigenbaum, Quantitative universality for a class of nonlinear transformations, *J. Stat. Phys.* 19 (1978) 25–52.
- [39] D. Ruelle, F. Takens, On the nature of turbulence, *Commun. Math. Phys.* 20 (1971) 167–192.
- [40] Y. Pomeau, P. Manneville, Intermittent transition to turbulence in dissipative dynamical systems, *Commun. Phys.* 74 (1980) 189–197.
- [41] R. Enns, G. Mc Guire, *Nonlinear Physics with Mathematica for Scientists and Engineers*, Birkhäuser, Boston, 2001.
- [42] J.C.R. Hunt, C.J. Abell, J.A. Peterka, H. Woo, Kinematic studies of the flows around free or surface mounted obstacles: applying topology to flow visualization, *J. Fluid Mech.* 86 (1) (1978) 179–200.
- [43] M.J. Lighthill, Attachment and separation in three-dimensional flow, in: L. Rosenhead (Ed.), *Laminar Boundary Layers*, Oxford University Press, 1963, pp. 72–82 (Chapter-II, Section 2.6).